RESEARCH ARTICLE | DECEMBER 03 2024

Flow characteristics induced by a multiform windbreak in complex terrains with and without a train: A simplified method for calculating aerodynamic loads

Special Collection: Flow and Civil Structures

Hongrui Gao (高鸿瑞) ; Tanghong Liu (刘堂红) ; Xiaodong Chen (陈晓栋) ; Haoyang Zeng (曾浩洋); Guang Chen (陈光) ; Zhengwei Chen (陈争卫) ; Jie Zhang (张洁) ; Boo Cheong Khoo

Physics of Fluids 36, 125115 (2024)
https://doi.org/10.1063/5.0236039

Physics of Fluids ARTICLE pubs.aip.org/aip/pof

Flow characteristics induced by a multiform windbreak in complex terrains with and without a train: A simplified method for calculating aerodynamic loads

Cite as: Phys. Fluids **36**, 125115 (2024); doi: 10.1063/5.0236039
Submitted: 30 August 2024 · Accepted: 5 November 2024 ·
Published Online: 3 December 2024

Hongrui Gao (高鸿瑞),[1,2,3,4] Tanghong Liu (刘堂红),[1,2,3,a)] Xiaodong Chen (陈晓栋),[1,2,3] Haoyang Zeng (曾浩洋),[1,2,3] Guang Chen (陈光),[1,2,3] Zhengwei Chen (陈争卫),[5] Jie Zhang (张洁),[1,2,3] and Boo Cheong Khoo[4]

AFFILIATIONS

[1]Key Laboratory of Traffic Safety on Track (Central South University), Ministry of Education, School of Traffic & Transportation Engineering, Central South University, Changsha 410075, China
[2]Joint International Research Laboratory of Key Technology for Rail Traffic Safety, Central South University, Changsha 410075, China
[3]National & Local Joint Engineering Research Center of Safety Technology for Rail Vehicle, Central South University, Changsha 410075, China
[4]Department of Mechanical Engineering, College of Design and Engineering, National University of Singapore, Singapore 117575, Singapore
[5]Department of Civil and Environmental Engineering, The Hong Kong Polytechnic University, Hong Kong 999077, China

Note: This paper is part of the special topic, Flow and Civil Structures.
[a)]**Author to whom correspondence should be addressed:** lth@csu.edu.cn

ABSTRACT

This study aims to investigate common multiform windbreaks, aligned parallel to railway tracks and perpendicular to incoming wind, in complex terrains. Using unsteady simulations, the study analyzes airflow downstream of these windbreaks and the aerodynamic characteristics during train passage. It evaluates the wind-protection performance of various windbreak types and transitions and identifies factors that influence performance. Results indicate that the vertical surface walls offer stronger wind protection compared to slope walls or viaduct barriers. Flow patterns near transitions reveal that upstream airflow shifts longitudinally from high-performance windbreaks to lower-performance ones, reentering the railway line space from the latter. This suggests a design approach in which neighboring windbreaks exhibit similar performance to optimize protection. On aerodynamic characteristics of the train, the maximum side force on the leading vehicle is found proportional to wind speed and train speed to the powers of 1.6 and 0.5, respectively; train speed affects the pressure on the streamlined head and the vortices around the leeward side. A simplified calculation for aerodynamic loads on a vehicle is proposed and explored with a consideration of wind speed above the railway line. An error margin of the maximum side force by this simplified method is 8.4%, and the saving is at least 88.2% of the computational resources when assessing the crosswind stability of a vehicle. The proposed design for the multiform windbreak, along with the simplified calculation method, can improve the performance of a multiform windbreak and increase the efficiency of assessing crosswind safety for railway operations downstream of the windbreak.

NOMENCLATURE

C_p	Pressure coefficient
CWC	Characteristic wind curve
F_D	Wind load (N)
H	Height of leading vehicle (m)
h_z	Height from top of rail (m)
LWL	Leeward line
p	Pressure (Pa)
p_0	Reference static pressure (Pa)
q	Dynamic pressure (Pa)
Q	Second invariant of velocity gradient tensor (s^{-2})

RCT	Railway cutting
SSW	Sloping-surface wall
U_0	Inlet wind speed (m s^{-1})
U_y	Wind speed in y direction (m s^{-1})
VSW	Vertical surface wall
v_{tr}	Train speed (m s^{-1})
WBV	Wind barrier on viaduct
w_p	Wind pressure (Pa)
WWL	Windward line
$y+$	Dimensionless wall distance

Greek letters

ρ	Air density (kg m^{-3})

I. INTRODUCTION

Crosswinds increase the aerodynamic loads on a train, on which the safety of railway operations depends.[1] There have been several train accidents such as derailment and overturning in crosswinds,[2–6] which caused grave losses of life and property. The maximum instantaneous wind speed recorded was 67 m/s near railways in Xinjiang, China. A train overturned in crosswinds in Xinjiang and killing of four passengers on 28 February 2007.[7–9]

Windbreaks, like windbreak walls and wind barriers, can decrease the aerodynamic loads on a train,[6,10–12] and is one of the most efficient and economic way to improve the crosswind safety of railway operations.[13,14] Windbreaks are mostly vertical surfaces or fences in Europe.[15–17] However, many windbreaks are made with local materials available near railways in Xinjiang due to complex terrain affecting the logistical transport and even construction. An example of a multiform windbreak developed in complex terrains[14,18–23] is shown in Fig. 1. Accordingly, there are six main kinds of windbreaks spread along the Southern Xinjiang Railway, and four for the Lanzhou–Urumqi High-speed Railway, including the cutting, earth-embankment wall, concrete wall, reinforced-concrete wall, wind barrier, and so on.

A windbreak can provide protection from wind, but the different flow downstream of different windbreaks leads to different protection performance.[14,21] Much work have been on the flow and aerodynamic characteristics of trains downstream of standalone windbreaks such as cuttings,[20,24,25] earth-embankment walls,[22,26] vertical surface walls,[27–32] and wind barriers.[13,33,34] However, a sudden change in the flow in a transition between two windbreaks may result in deterioration of the aerodynamic and dynamic performance of a train.[35–39] Hence, the crosswind stability of vehicles downstream of the multiform windbreaks cannot be readily assessed just based on the cases of standalone windbreak.

Studies on full-scale tests and numerical simulations on the aerodynamic characteristics of vehicles passing by transitions between different windbreaks are broadly summarized in Table I. Although the full-scale test can measure the aerodynamic loads and surface pressure on a vehicle passing by a windbreak transition in the real environment, it is not the norm because of high costs, strict operating conditions, difficulties of obtaining permit, and other measurement challenges.[40,41] With the rapid development of computer, it is far easier to obtain the aerodynamic characteristics of a vehicle passing by a windbreak transition via numerical simulation than the full-scale test,[42] and the results can also be reliable especially after verification. Furthermore, the numerical simulation enables researchers to obtain more and complete information about the flow vis-a-vis the limited field measurements.[25] However, most numerical simulations have thus far mainly focused on the aerodynamic characteristics of a vehicle passing by a transition between two windbreaks instead of a multiform windbreak in complex terrains. Also, the aerodynamic loads of a vehicle passing by a windbreak transition at different wind speeds and train speeds need to be simulated to assess the crosswind stability of the vehicle, and it is very resource intensive too.

In this work, the flow dynamics and aerodynamic characteristics of a train passing by a multiform windbreak in the complex terrains along the Southern Xinjiang Railway are simulated. The wind-protection performance of the windbreaks is thoroughly evaluated, and key factors influencing the train's aerodynamic characteristics are analyzed. Additionally, a simplified method for calculating the aerodynamic loads on the vehicle, based on the wind speed field above the railway line, is investigated.

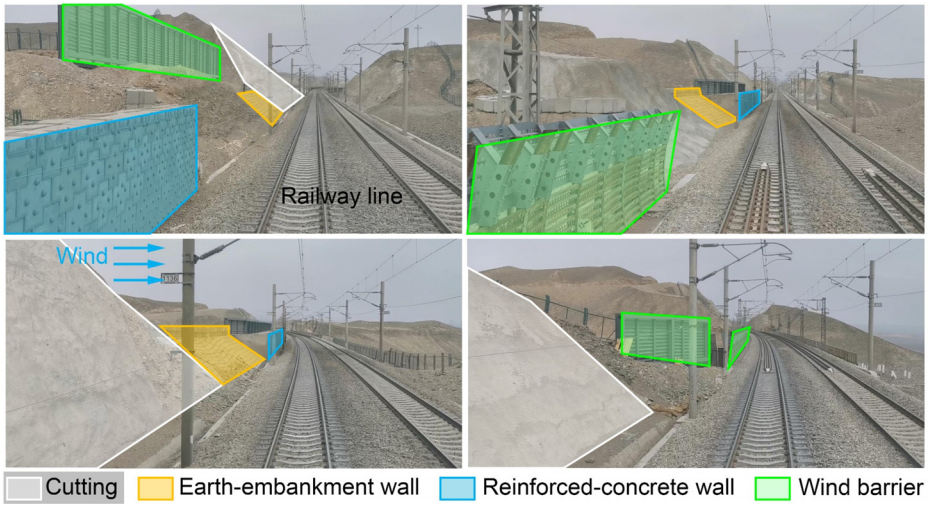

FIG. 1. Multiform windbreak in complex terrains along Southern Xinjiang Railway in China.

TABLE I. Aerodynamic characteristics of vehicles passing by transitions between windbreaks in previous full-scale tests and numerical simulations.

Means	References	Transitions between windbreaks	Aerodynamic characteristics
Full-scale tests	Gao *et al.*[43]	Cutting and earth-embankment wall	Aerodynamic loads and surface pressure
	Liu *et al.*[44]	Cutting, earth-embankment wall, reinforced-concrete wall, and wind barrier	Aerodynamic loads
	Wei *et al.*[45]	Opening in concrete wall	Surface pressure
	Liu *et al.*[19]	Cutting and concrete wall	Aerodynamic loads, surface pressure, and flow
Numerical simulations	Chen *et al.*[35]	Cutting and concrete wall	Aerodynamic loads and flow
	Deng *et al.*[18]	Concrete wall and wind barrier	Flow
	Sun *et al.*[46]	Opening in concrete wall	Aerodynamic loads and flow
	Liu *et al.*[47]	Opening in reinforced-concrete wall	Aerodynamic loads

The primary contributions of this work are twofold:

(1) **Pressure-driven longitudinal flow and windbreak design:** This work reproduces pressure-driven longitudinal flow upstream of windbreaks, which reduces the wind-protection performance at transitions between different windbreak types. Based on these findings, a design concept for a more reliable multiform windbreak is proposed.
(2) **Simplified aerodynamic load calculation:** By analyzing flow characteristics downstream of windbreaks with and without a passing train, a simplified method for calculating aerodynamic loads on vehicles is introduced. This method significantly improves the efficiency of assessing the crosswind stability of vehicles passing through areas protected by multiform windbreaks.

Section II details the computational fluid dynamics approach and full-scale tests conducted for verification. The results from these simulations and the proposed simplified method are presented and analyzed in Sec. III. Finally, Sec. IV provides a summary of the main findings.

II. METHODS

A. Numerical simulations

1. Train and topography models

As shown in Fig. 2(a), the train model is consistent with the tested train in our previous full-scale tests,[43] but is simplified into a five-vehicle composition. The train model is 128.207 m long. The base of the wheel is cut to avoid numerical singularities in the contact point between the wheel and rail.[16] Figure 2(b) represents the leading vehicle, including the tested vehicle in the full-scale tests[43] (see Sec. II B) and the vehicle model in the numerical simulations. The vehicle height is H (= 4.433 m), and its length is 28.5 m. The bottom of the vehicle model is basically in line with the reality.

Figure 3(a) shows the real topography in this work, a typical region with a complex terrain and a multiform windbreak on Southern Xinjiang Railway in China. Figure 3(b) shows the topographic model in the simulations, obtained by unmanned aerial vehicle measurement and three-dimensional modeling.[48] The root mean square deviation of the contour lines of the topographic maps by unmanned aerial vehicle measurement is no greater than 0.7 m, which meets the Chinese Standard.[49] Considering both the computational resources and the impact of small geometric features on the aerodynamic characteristics of the train, the topography, windbreaks, and railway lines[50] are properly simplified and reconstructed. The topographic model is 581 m long, and its degree of relief is 144 m. Similar topographic data are also available in electronic form at the Geospatial Data Cloud held by Computer Network Information Center, Chinese Academy of Sciences.

Figure 4(a) illustrates the four types of windbreaks used in this work: railway cutting (RCT), sloping-surface wall (SSW), vertical surface wall (VSW), and wind barrier on viaduct (WBV). The RCT is a narrow open passage dug through high ground or a hill. The SSW and VSW are solid structures (with a porosity of 0%), while the WBV is a porous structure with a porosity of 21.6%. Additionally, a porous wind barrier is positioned upstream of the VSW. To manage computational resources, the hole diameter on the wind barriers is enlarged to 240 mm while maintaining consistent porosity. It leads to a worse wind-protection performance,[33] which indicates that the results are conservative in this work. The RCT is positioned on both sides of the railway line, whereas the SSW, VSW, and WBV are located only on one side and upstream of the line. The distance and heights of these windbreaks are specified in Fig. 4(a). The height of the RCT depends on the height of the surrounding high ground or hill, ranging from 2.343 to 18.688 m.

The railway line closer to windbreaks is referred to as the windward line (WWL), and the line farther away is the leeward line (LWL). In this work, the train runs on the WWL (see Sec. III B 1), and the distance between the centerlines of the WWL and LWL is 4.4 m. The ballast and rail configuration follows the European Standard.[16] To maintain a consistent rail height in complex terrains, embankments and viaducts (not shown) are constructed where necessary.

Figure 4(b) depicts the distribution of the multiform windbreaks along the railway line. The windbreaks include the RCT, SSW, VSW, and WBV, which make up 25.3%, 9.3%, 28.2%, and 31.7% of the total length, respectively. The colors used in the figure—white for RCT, yellow for SSW, blue for VSW, and green for WBV—correspond to these windbreak types and will be used consistently in later sections. The figure also indicates the distances from the origin O to the locations of the transitions between different types of windbreaks (hereafter

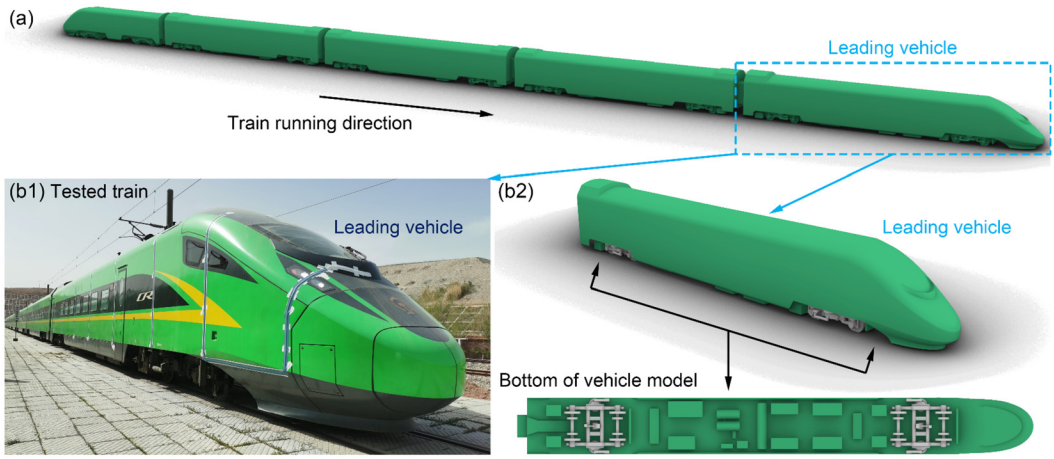

FIG. 2. (a) Train model and (b) leading vehicle.

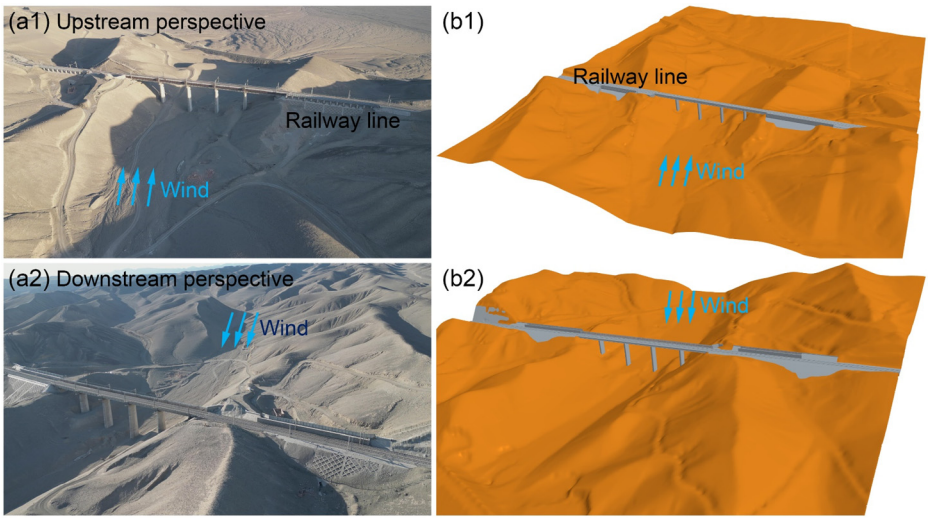

FIG. 3. Topography in (a) reality and (b) simulations.

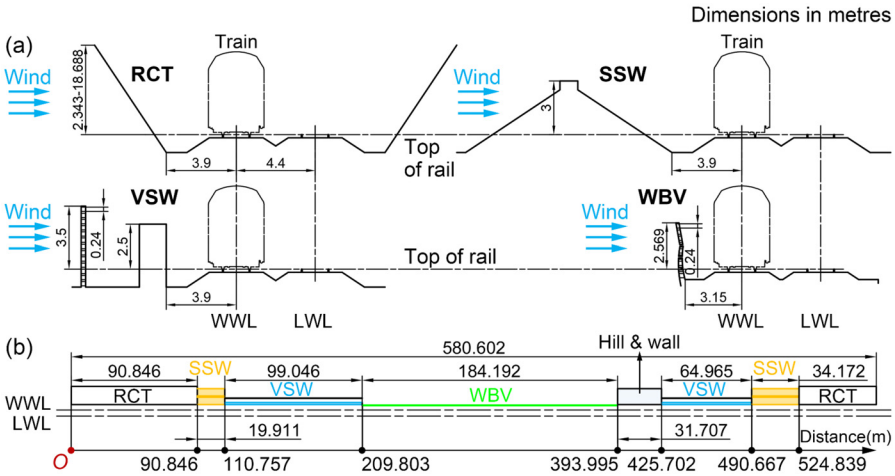

FIG. 4. (a) Different windbreaks and (b) their layout.

referred to as distance). At the distance between 393.995 and 425.702 m (between the WBV and VSW), there is a hill with a maximum height of approximately 5.5 m above the top of the rail. This topographical feature is significant as it influences the flow characteristics and the effectiveness of the windbreaks in this region.

Figure 5(a) illustrates the transitions between different types of windbreaks along the railway line. These transitions are crucial in determining the wind-protection performance and the aerodynamic characteristics of the train passing by. The key details of the transitions are as follows:

- **Transition between RCT and SSW:** There is no gap at this transition.
- **Transition between SSW and VSW:** A wall is constructed perpendicular to the railway line to fill the gap at this transition.
- **Transition between VSW and WBV:** A gap of 298 mm exists at this transition due to the closer proximity of the WBV to the WWL.

Figure 5(b) illustrates the windbreak transitions at various distances along the railway line. These simulated transitions closely mirror those found in real-world scenarios, ensuring that the results are applicable to actual railway operations in complex terrains. In Fig. 5(b3), the gaps between the hill and nearby windbreaks have been filled to the best of the engineers' ability.

This study focuses on analyzing flow characteristics downstream of a multiform windbreak in complex terrain. The selected section features varied windbreak types, frequent transitions, and intricate surrounding topography. As noted in Sec. I, the windbreak types illustrated in Fig. 4 correspond to specific topographic features in their immediate areas. Such multiform windbreak structures are prevalent along railways in the wind-prone regions of Xinjiang, China.

2. Computational domain and boundary conditions

Figure 6 presents the computational domain. The model dimensions are at full scale. To prevent or mitigate the domain boundaries

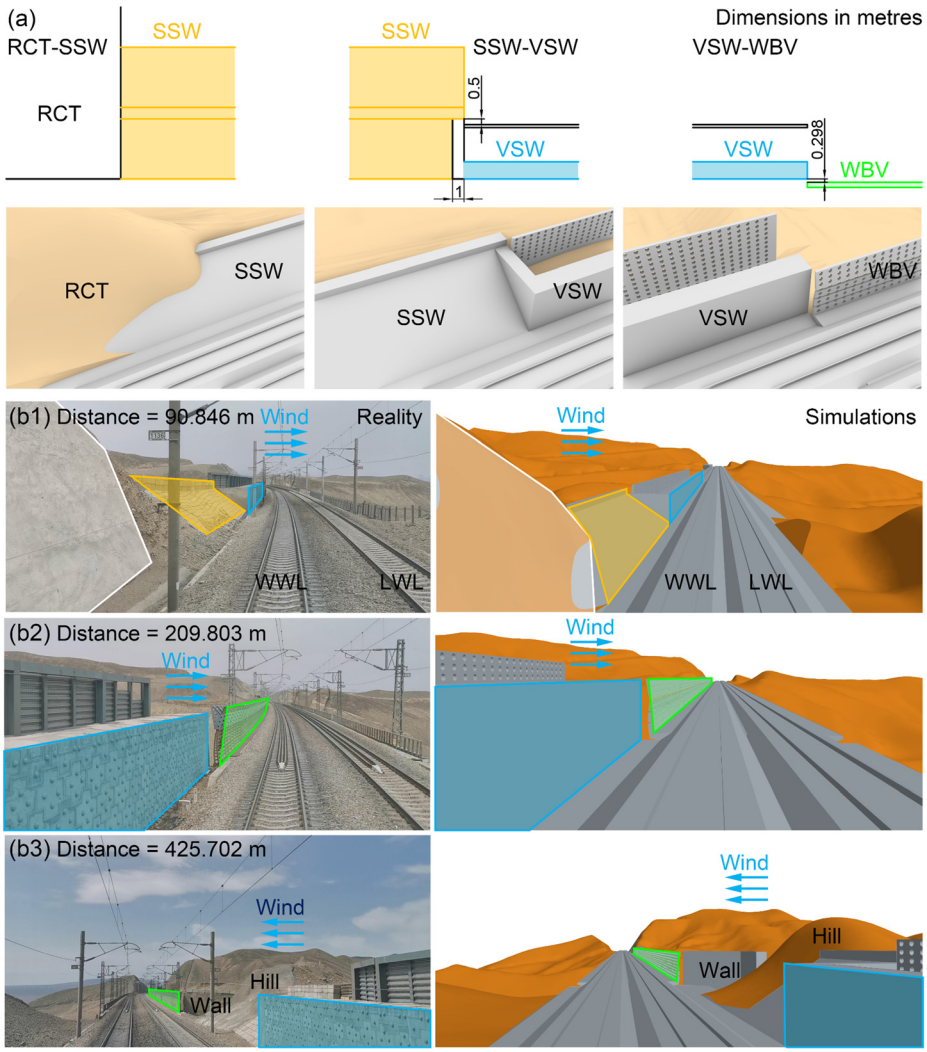

FIG. 5. Windbreak transitions: (a) transitions between different windbreaks and (b) transitions in complex terrains in reality and simulations.

from interfering with the flow above the topography in a physically incorrect/unrealistic way and ensure that the train runs through the topographic domain, the model is stretched longitudinally by 500 m (in the positive and negative x-directions), bringing the total length of the computational domain to 1581 m. The distances from the longitudinal center plane of the railway line to the computational boundaries upstream and downstream are 256 and 530 m, respectively. The width of the domain is 786 m. The height of the domain is 417–561 m (due to topographic relief). The blockage ratio is less than 5%, which meets the European Standard.[16]

Figure 6 also shows the boundary conditions. The upstream computational boundary of the railway line is a velocity inlet (toward computational domain Face ABCD). The onset wind is parallel to the slope (at the slope angle of about 5°). The "inlet wind speed" is the velocity in the general y direction at the velocity inlet. Often two-dimensional anemometers are used to measure the wind speed near the railway lines. The computational downstream boundary is a pressure outlet (Face EFGH) with the constant (gauge) pressure of 0 Pa. The top and lateral plane boundary conditions are slip walls (Face ABFG, ADHG, and BCEF). The ground and the surfaces of the train, windbreaks, and lines are treated as no-slip walls, and the roughness height of the ground is 0.07 m. The train is initially in the stretch in the positive x direction, and the nose of the leading vehicle is 125 m from the origin in the x direction. The train runs in the minus x direction.

3. Computational mesh

The computational meshes include trimmed meshes[51] and prismatic cell layers next to the no-slip wall boundaries. Figures 7(a) and 7(b) represent the cell sizes on and adjacent to the surfaces of the leading vehicle and the WBV, respectively. The dimensionless wall distance $y+$ for the first cell layer meets basic requirements in the European Standard[16] and matches the turbulence model (see Sec. II A 4). The number of prism layers on the surface of the leading vehicle is 10, and its growth rate is 1.2.

Figure 7(c) presents the size and distribution of the computational cells for the different windbreaks. The mesh can capture regions of high pressure/velocity gradient. The number of cells is 113 million. Our previous work[43] has proven mesh independency for the leading vehicle.

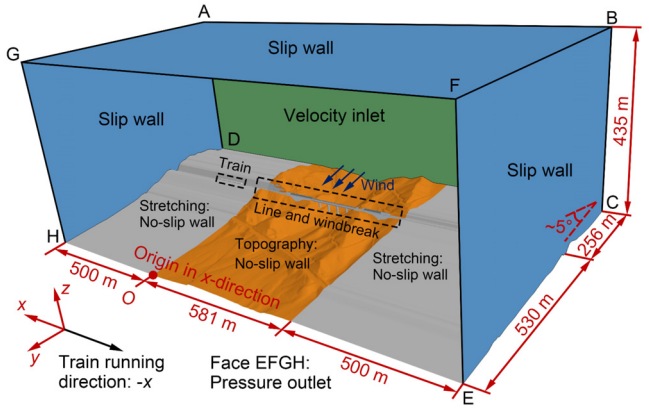

FIG. 6. Computational domain and boundary conditions.

4. Computational method and turbulence modeling

The numerical simulations have a background region enclosing the entire computational domain and a smaller overset region containing the train in this work. Whenever the position of the overset region changes, some of the cells in the background region are closed, and then, the solution is computed for all active cells in all regions simultaneously.[51]

The unsteady Reynolds-averaged Navier–Stokes method is used, which can model the viscous, turbulent, unsteady, three-dimensional, and strongly separated flows. Previous studies[19,35,46,52] have used this method to simulate the aerodynamic characteristics of trains passing by windbreak transitions and yielded reliable results. The turbulence model is the realizable k–ε model. There are two reasons these calculation method and turbulence model are used. First, this work mainly focuses on the trend of the aerodynamic loads of the vehicle affected by the multiform windbreak in complex terrains rather than the quantitative fluctuating component caused by the inlet and local turbulence. Second, it is a balance of the computing accuracy and cost.[51,53]

The numerical simulations are divided into two periods:

- **Wind speed simulation (without a train):** The wind speeds above the railway line were simulated firstly with the static train model and a physical time step of 0.01 s. There were 2000 steps. The train was stationary at the initial position (the stretch in the positive x direction) in Fig. 6, and there was no train in the topography. The result is shown in Sec. III A.
- **Aerodynamic load simulation (with a moving train):** The aerodynamic characteristics of the train model were then simulated at the train speed of one minimum cell size per time step (for better coupling of the background and overset regions). There were 5200 steps. The train crossed the topography starting at the initial position. The result is shown in Sec. III B.

The wind speed simulation and the aerodynamic load simulation were carried out on 16 Intel® Xeon® Gold 6248R Processors and consumed about 4224 core hours and 15744 core hours (individual simulations), respectively.

B. Full-scale tests

Eight full-scale tests were conducted on the Southern Xinjiang Railway in China from March to April 2021. The tested train [see Fig. 2(b1)] and force measurement are identical to our previous full-scale tests.[43] The accuracy of this force measurement has been proved and verified.[54] These test results provide preliminary data for analyzing aerodynamic forces on the train and serve as a basis for validating the numerical simulations. During testing, the train traveled on the WWL [see Fig. 2(b1) for the leading vehicle] at maximum speeds ranging from 54 to 145 km/h. Maximum wind speeds, recorded at a nearby anemometer tower over 10-min intervals, reached 32.7–43.6 m/s, with the angle between the railway line and mean wind direction measured at 80.0°–83.9°.

III. RESULTS AND DISCUSSION

A. Flow characteristics without a train

The aerodynamic loads on a train passing by a multiform windbreak in complex terrains can be effectively correlated with the flow at the same position downstream of the windbreaks, specifically on the

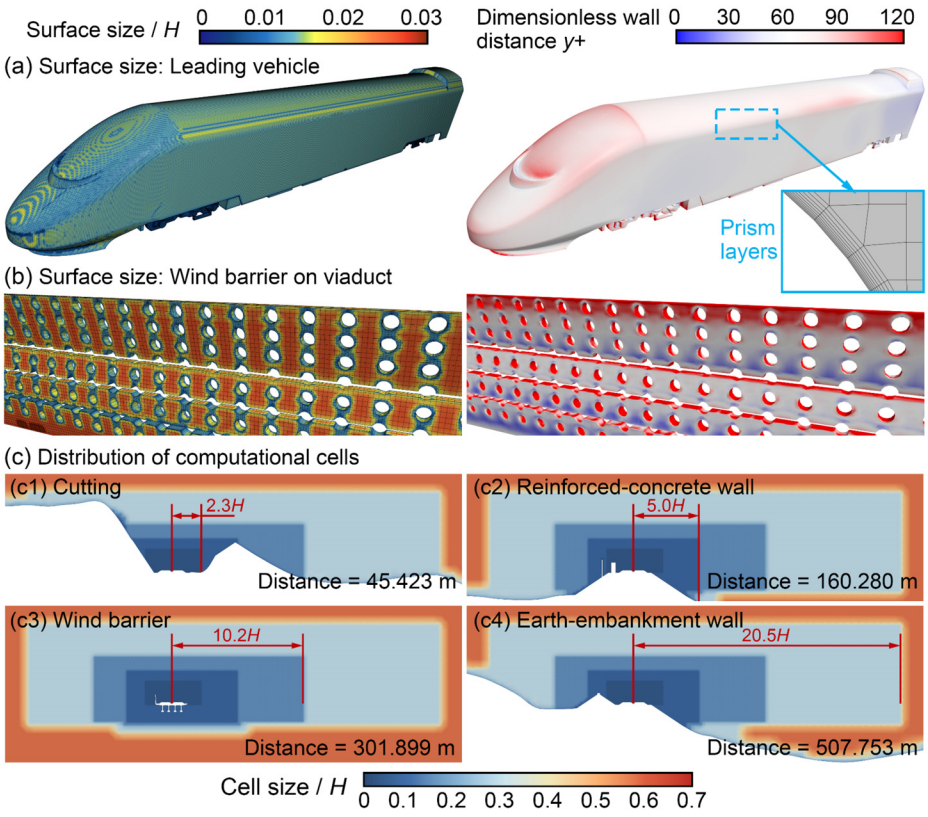

FIG. 7. Size of wall surface on (a) leading vehicle and (b) wind barrier on viaduct and (c) distribution of computational cells.

railway lines, when there is no train present. This section focuses on analyzing the flow near the lines and windbreaks without a train.

The downstream flow characteristics of the various windbreak types in this study have been previously measured through field measurements and wind tunnel tests. Full-scale tests on RCT were reported by Liu *et al.*,[19] field measurements on SSW were reported by Dong *et al.*,[55] and wind tunnel tests on VSW and WBV were detailed by Gu *et al.*[30,56] and Liu *et al.*,[33] respectively. These previously reported results are referenced here for context and will not be reiterated in this work.

Our previous works[35,36,57] have established the validity and accuracy of the simulation approach used in this work in complex terrains without the presence of a train.

1. Wind speed distributions above railway lines

Figures 8(a) and 8(b) depict the normalized wind speeds, i.e., the ratio of the local horizontal wind speed to the inlet wind speed, at the heights of H (= 4.433 m) and $0.5H$, respectively, above the top of the rail. These heights are chosen because the wind speeds at elevations corresponding to or below the vehicle height are most likely to influence the aerodynamic loads on a train passing by the windbreak. The distribution of normalized wind speeds is consistent across different inlet wind speeds; therefore, the analysis focuses on the case with an inlet wind speed of 30 m/s. The figures illustrate low-speed regions (indicated by blue areas) downstream of the windbreaks. The low-speed areas at the height of $0.5H$ are more extensive than those at the height of H, and the areas downstream of the SSW and VSW are larger compared to those downstream of the WBV. These low-speed regions serve as an indicator of the protection performance of the windbreaks. The larger these low-speed areas are, the more effectively the windbreak is mitigating wind impact on the railway line.

Figures 8(c) and 8(d) provide a quantitative analysis of the normalized wind speeds above the WWL and LWL as depicted in Figs. 8(a) and 8(b), respectively. Wind speeds at the height of $0.5H$ above the top of the rail are generally lower than those at the height of H. The normalized wind speed at the height of H above the WWL downstream of the WBV exceeds one; the accelerated flow in the valley[58] and around the WBV[13,33] make the wind speed above the WWL higher than the inlet wind speed. The wind speed above the LWL is noticeably lower, which is likely because it is less affected by the accelerated flow that passes over the WBV. A particularly high wind speed is observed near the distance of 45.423 m, corresponding to the RCT. This effect is especially pronounced at the height of $0.5H$ above the LWL. Locations near the transitions between different windbreaks also experience relatively high wind speeds. Although these wind speeds are slightly higher than the inlet wind speed, they are lower than the wind speed above the WWL downstream of the WBV. The low wind speeds observed above the railway line in certain areas can be attributed to the strong protection provided by the windbreaks. From the analysis, the VSW demonstrates stronger/better wind-protection performance compared to the SSW and WBV, confirming similar findings from other studies, such as those by Zhang *et al.*[14]

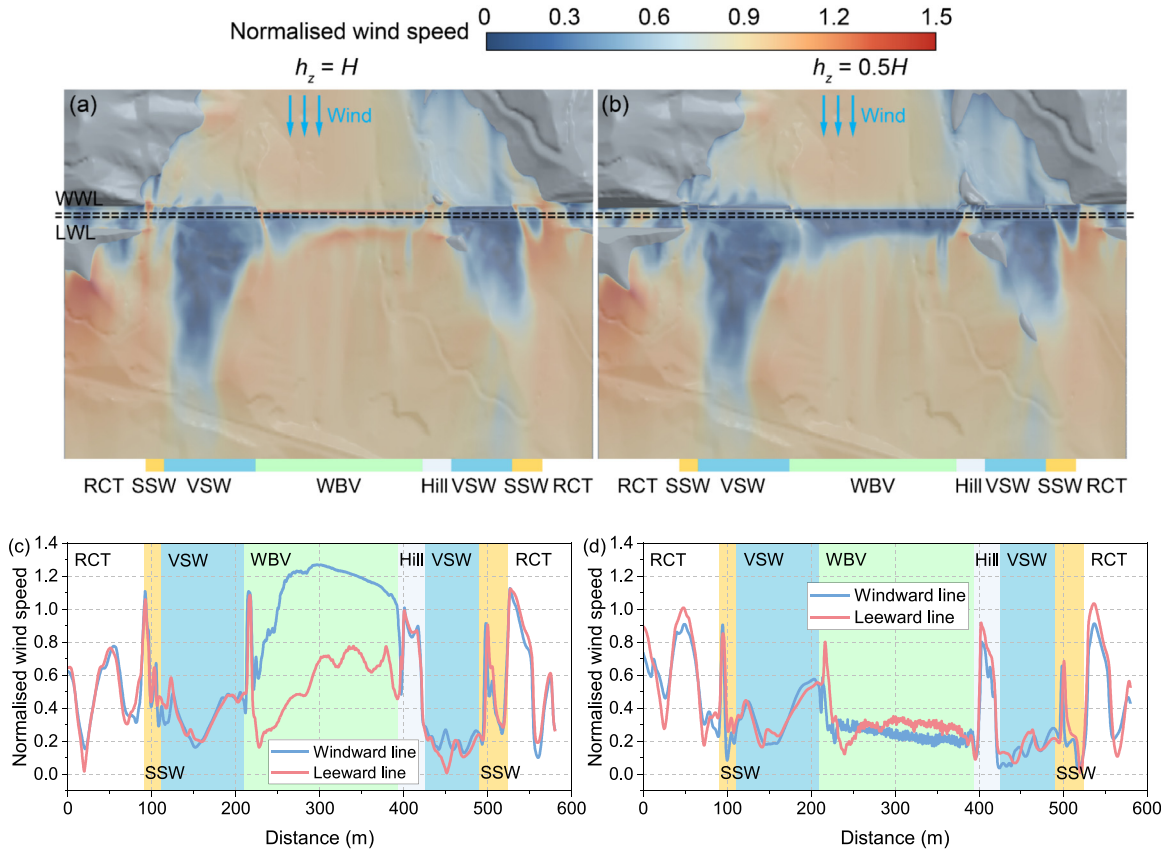

FIG. 8. Normalized wind speeds without train at heights above top of rail at: (a) *H* (plan view) and (b) 0.5*H* (plan view), and those along windward and leeward lines at heights above top of rail at: (c) *H* and (d) 0.5*H*.

2. Flow near individual windbreaks

Figures 9(a) and 9(b) show the wind speed distributions and two-dimensional streamlines at the locations with weak wind-protection performance, specifically in the SSW, WBV, and hill regions. The WBV's poor performance is primarily due to its low height [see Fig. 4(a)], which allows the inlet wind to enter readily over the range of the railway line [see Figs. 9(b1) and 9(b2)]. Additionally, some of the wind passes through the holes in the WBV, directly entering the range of the railway line and affecting the recirculation downstream of the WBV.[13,14,33] Consequently, the WBV provides better protection for the LWL compared to the WWL, as reflected in the wind speed patterns shown in Fig. 8(c). At the distance of 404.75 m [near the hill, see Fig. 9(b3)], the windbreak's poor performance is due to its low effective height, caused by the hill upstream. The wind rushing down from the hill passes over the windbreak and enters the range of the railway line, resulting in wind speeds above the line similar to those at the inlet. Next, the SSW's ineffective performance stems from its weak ability to lift the inlet wind [see Fig. 9(b4)], which is related to its aerodynamic design. The inlet wind flows up the slope, over the top of the wall, and then descends,[21] resulting in minimal recirculation downstream of the wall. As a result, the SSW is more effective at protecting the WWL than the LWL. In summary, these windbreaks have a weak ability to raise the inlet wind, due to their aerodynamic configuration or low effective height. This allows the wind to flow along and over them, entering the range of the railway line.

Figure 9(c) provides a quantitative analysis of the normalized wind speeds at different heights above the WWL and LWL, as shown in Fig. 9(b). The results corroborate with earlier discussions on the weak wind-protection performances of the WBV and SSW. The wind speed distributions downstream of the WBV, particularly in Figs. 9(c1) and 9(c2), show significant differences. The distribution in Fig. 9(c2) aligns with findings from previous studies.[13,33] Three key factors likely contribute to these variations. First, the distance of 212.75 m is close to the transition between the VSW and WBV, where the flow along the railway line might influence wind speed distributions in Fig. 9(c1). Second, the beginning part WBV at the distance of 212.75 m has limited number of holes, whereas the WBV at the distance of 308.75 m has more. This structural variation can cause differences in wind speed distributions, especially below the top of the WBV. Finally, the distances of 212.75 and 308.75 m correspond to one end of the viaduct and its middle, respectively. Variations in the vertical wind speed distribution in the valley[58] and differences in the shape of the T-beams [see Figs. 9(b1) and 9(b2)] further contribute to the variations in wind speed distributions above the line. At the distance of 404.75 m [the hill, as shown in Fig. 9(c3)], the wind speed distribution above the railway line resembles that of an atmospheric

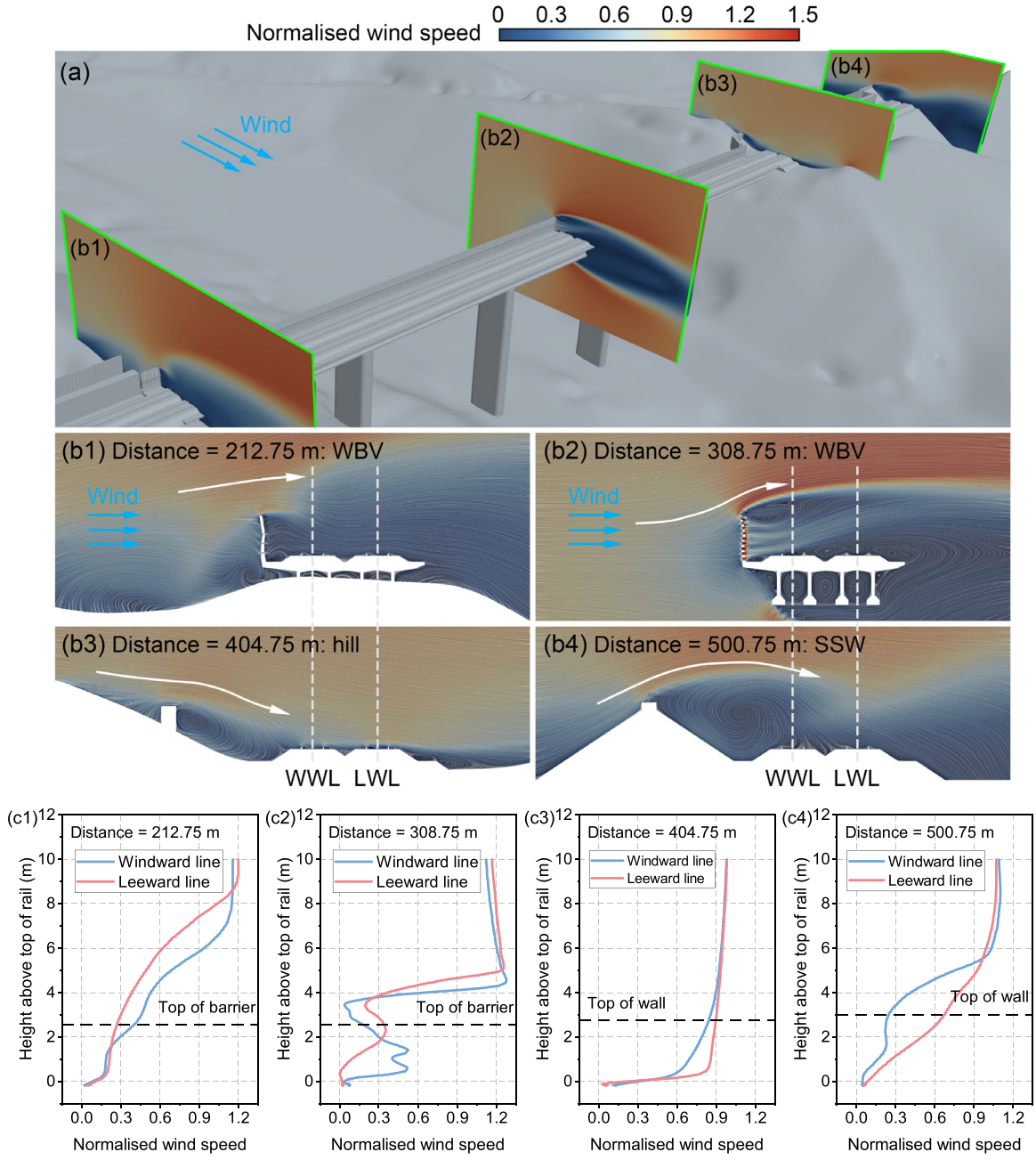

FIG. 9. (a) Different locations along railway line, normalized wind speeds and streamlines at distances of: (b1) 212.75, (b2) 308.75, (b3) 404.75, and (b4) 500.75 m, and normalized wind speeds at different heights at distances of: (c1) 212.75, (c2) 308.75, (c3) 404.75, and (c4) 500.75 m.

boundary layer, indicating that the inlet wind directly influences the wind speed above the line, pointing to weak wind-protection performance at this location. The wind speed distribution at the distance of 500.75 m (the SSW) closely resembles a simulation by Yang *et al.*,[22] where the flow suddenly accelerates above the top of the wall.

As shown in Fig. 9(c), the vertical distributions of wind speed are complex, making it challenging to accurately represent the overall wind speed distribution above the railway line via measurements taken at individual heights and locations.

3. Flow near windbreak transitions

Figures 10(a) and 10(b) show the topography and three-dimensional streamlines near the locations subject to high wind speeds

as identified in Figs. 8(c) and 8(d), respectively. The three-dimensional streamlines are colored according to the normalized wind speed, revealing the flow dynamics in these critical regions. Near the distance of 45.423 m, the height of the RCT begins to decrease. This reduction in height causes the flow passing the cutting shoulder to accelerate and directly enter the range of the railway line. With the leeward-cutting block, the flow accelerates again above the LWL [the wind speed here above the LWL is higher than that above the WWL, as shown in Fig. 8(d)]. The accelerated flow exits the RCT along the railway line, contributing to high wind speeds near the distance of 90.846 m, where the transition between the RCT and SSW occurs. The relatively weak ability of the SSW to deflect and slow down the inlet wind allows the accelerated flow to enter the railway line range, further intensifying the wind speed in this transition zone.[14,21,26] In Figs. 10(b3) and 10(b5), the streamlines illustrate how the flow upstream of the windbreaks tends to move longitudinally from stronger-performing windbreaks to weaker ones. Specifically, the flow moves from the VSW to both the WBV and the SSW. This directional flow indicates that the VSW, having stronger wind-protection performance, pushes the wind toward the adjacent, less effective windbreaks.

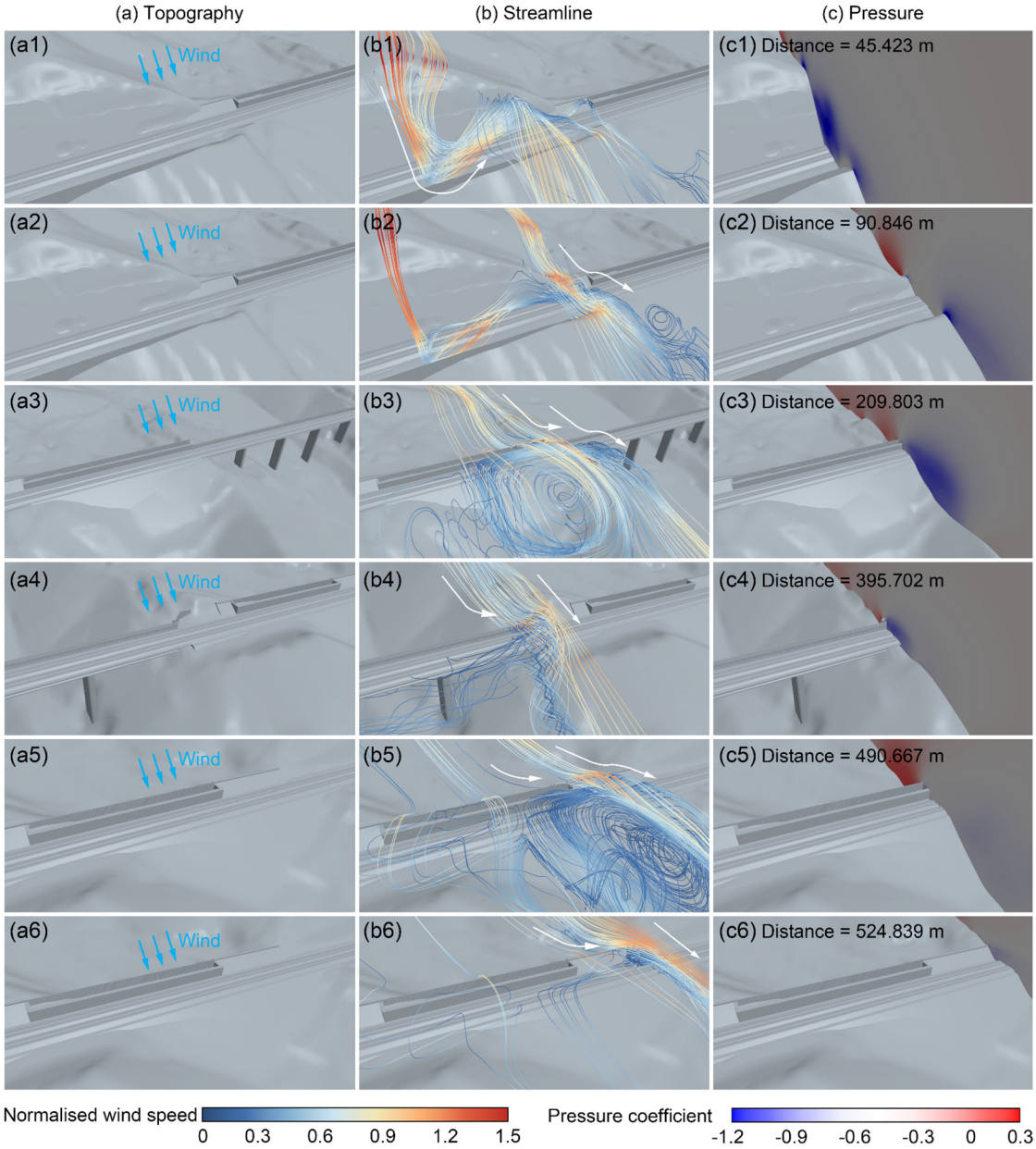

FIG. 10. (a) Topography, (b) streamlines, and (c) pressure at different locations along railway line.

Figure 10(c) represents the air pressure near the locations where high wind speeds were previously identified, and where the pressure coefficient C_p is calculated from the following:

$$C_p = \frac{p - p_0}{q}, \tag{1}$$

$$q = \frac{\rho U_0^2}{2}. \tag{2}$$

Here, p and p_0 are the pressure and reference static pressure, respectively; q is the dynamic pressure; ρ is the air density; and U_0 is the inlet wind speed. Positive/increased pressures is observed upstream of the windbreaks, primarily due to the windbreaks obstructing the incoming wind. The presence of significant positive pressure upstream of a windbreak suggests that it effectively disrupts the incoming flow, contributing to its protective performance. Negative pressure regions, found above the railway line, are linked to the recirculation zones that form downstream of the windbreaks. A pronounced negative pressure above the line indicates strong recirculation, further confirming the effectiveness of the windbreak. The significant positive pressure upstream of the windbreaks, particularly near the transitions, helps explain the longitudinal movement of the flow upstream of the windbreak transitions. At the distance of 524.839 m, where the transition between the SSW and RCT occurs, Fig. 10(c6) reveals the absence of significant positive pressure upstream of the windbreak and a lack of visible negative pressure above the railway line. This lack of pressure indicators suggests that the windbreak's protection performance is relatively weak at this transition. This finding is consistent with the wind speed distributions in Figs. 8(c) and 8(d), where higher wind speeds are observed in this area.

Based on the wind speeds at the heights of H and $0.5H$ above the top of the rail, as well as the pressure distribution around the windbreaks, the general hierarchy of windbreak protection performance is as follows:

(1) **VSW:** Offers the strongest protection.
(2) **SSW/WBV:** These windbreaks offer moderate protection, with performance levels that are roughly equivalent to each other. **Transitions between different types of windbreaks:** These
(3) areas have the weakest protection, making them critical points of vulnerability.

For the **RCT**, its protection performance is directly related to its height. The taller the RCT, the more effective it is in protecting the railway line from crosswinds.

The diminished wind-protection performance observed at the windbreak transitions can be attributed to the disparity in protection capabilities between the adjoining windbreaks. This difference in performance results in varying pressure levels upstream of each windbreak. Specifically, the windbreak with stronger protective capabilities generates high-pressure region, while the weaker one creates relatively low-pressure region. This pressure differential drives the wind flow (upstream of the windbreaks) to move longitudinally from the more effective windbreak to the less effective one, eventually reentering the railway line's vicinity over the weaker windbreak. Figure 11 illustrates this pressure-driven longitudinal flow upstream of each windbreak transition and highlights the areas of increased wind exposure above the railway lines. These exposures correspond to the high wind speed regions identified in Figs. 8(c) and 8(d).

The areas experiencing high wind speeds in Figs. 8(c) and 8(d) do not precisely coincide with the transitions between the windbreaks. Instead, they tend to shift toward regions where the windbreak provides weaker protection, such as the areas around the SSW and WBV. High wind speeds are absent downstream of the VSW, which offers the strongest protection, even near the transitions. This can be attributed to the movement of the inlet wind from windbreaks with stronger protection to those with weaker performance. The RCT has a low height of 2.343 m near the distance of 524.839 m, where the transition between the SSW and RCT occurs [as seen in Fig. 10(b6)]. This lower height allows more wind to pass over the RCT and enter the railway line's range, resulting in the highest wind speed being observed at this location. This behavior aligns with previous studies.[21,24,59]

This pressure-driven longitudinal flow upstream of windbreaks sheds light on phenomena observed in previous studies. For instance, simulations by Chen *et al.*[35] revealed that the location experiencing the maximum wind speed downstream of a transition between a VSW and a RCT is near the low RCT, which offers weaker wind protection. This effect is attributed to the upstream flow moving longitudinally from the VSW to the RCT, as evident in their streamline data. To mitigate this, additional windbreaks were installed downstream of the RCT. The wind speed distribution above the railway line observed in their study resembles the distribution found near the RCT-SSW transition in this study. Similarly, simulations by Deng *et al.*[18] demonstrated that high wind speeds downstream of a transition between a VSW and a WBV occur near the WBV, where wind protection is less effective. The wind speed distribution above the railway line they reported aligns closely with what was observed near the VSW-WBV transition in this study.

In summary, the strength of an individual windbreak's protection may not be as crucial as ensuring that overall performance of a multiform windbreak is consistent. The effectiveness of the system is enhanced when each windbreak's performance aligns closely with that of its neighboring windbreaks, creating a more reliable windbreak.

B. Aerodynamic characteristics of moving trains

1. On full-scale test results and verification

Due to the variability of train and wind speeds in the full-scale tests, this section examines the maximum aerodynamic forces (side force and lift) on the leading vehicle (the tested vehicle) as well as the highest recorded train speed and the highest recorded wind speed within each 10-min test period. A subset of test conditions matching those in the numerical simulations was selected for verification purposes. Since the topography model's longitudinal edges are artificially extended along the positive and negative x axis in the simulations, the surrounding terrain in these areas differs from actual terrain. Therefore, to provide a more accurate comparison between the full-scale and simulation results, the maximum aerodynamic forces here exclude those acting on the vehicle in the RCT section.

Figure 12(a) shows the relationship between maximum aerodynamic force on the leading vehicle and peak wind speed, while Fig. 12(b) illustrates the correlation with maximum train speed. Error bars indicate measurement uncertainty, with mean uncertainties of 2.50 kN for side force and 2.94 kN for lift. A positive correlation is observed between aerodynamic force and wind speed, with correlation coefficients of 0.576 and 0.539 for side force and lift, respectively.

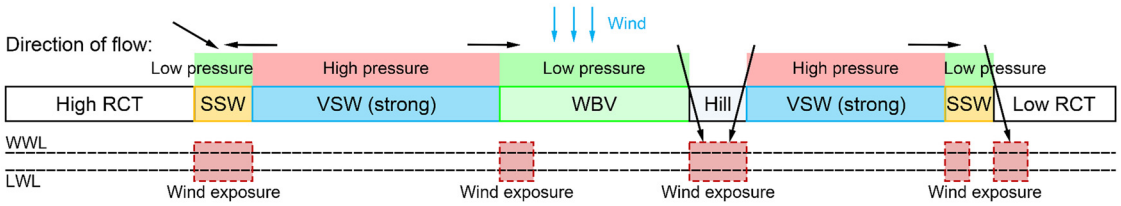

FIG. 11. Schematic of pressure-driven longitudinal flow upstream of windbreaks and areas of high wind exposure above railway lines.

Conversely, aerodynamic force shows a negative correlation with train speed, with coefficients of −0.574 and −0.324 for side force and lift. This inverse relationship arises because the train speed was reduced in higher wind conditions to ensure crosswind stability, meaning that higher wind speeds corresponded to lower train speeds. Consequently, wind speed is the dominant factor affecting aerodynamic force, resulting in an apparent negative correlation between train speed and aerodynamic force. However, it is reasonable to assume a positive underlying correlation between train speed and aerodynamic force, although wind speed exerts a greater influence.

Due to the complexity of controlling variables in real-world conditions, further insights into the impact of inlet wind and train speeds on aerodynamic loads are explored through numerical simulations (see Secs. III B 2 and III B 3). The inherent atmospheric variability and transient flows in the full-scale tests result in discrete data points,[40,60,61] a common outcome in previous tests[43] and an aspect underscoring the value of numerical simulations in this study.

Figures 13(a1) and 13(b1) show where the maximum side force and lift on the leading vehicle occur, respectively. The horizontal axis represents the distance between the midpoint of the leading vehicle and the origin (see Fig. 6), which is identical schematically to Fig. 4(a). The color-coded areas denote different windbreak types, as explained in Sec. II A 1. The highest side force on the leading vehicle was concentrated at the distance of 350–500 m, with a median of 400 m, downstream of the hill [transition between WBV and VSW, as shown in Fig. 13(a2)], aligning with the wind-exposure region in Fig. 11. Similarly, the maximum lift was observed at the distance of 350–400 m, with a median of 385 m, downstream of the WBV, as illustrated in Fig. 13(b2).

For verification, test results with similar wind and train speeds to this study were selected. In this test, the train ran on the WWL at a maximum speed of 77 km/h, with a 10-min peak wind speed of 35.5 m/s measured at a nearby anemometer tower and an 80.0° angle between the railway line and mean wind direction. Measurement uncertainties for side force and lift were 0.88 and 1.01 kN, respectively. Figure 14 presents aerodynamic forces from the numerical simulation and full-scale test, where error bands are measurement uncertainties. The topographic model is artificially stretched, as described in Sec. II A 2, which leads to differences between the topography depicted here and the ground. Hence, there are some differences between aerodynamic forces from the simulation and test. The difference is much less at region directly downstream of the SSW, VSW, WBV, and hill; the differences of the maximum side force and lift are 1.3% and −1.2% (see Table II), respectively. In addition to the topography, the differences are also attributed to complex external conditions in the full-scale test. First, the train speed and wind speed are strictly not constant in the full-scale test, and the maximum train speed and wind speed served as input to the simulation. Second, roll and vibrations of the vehicle caused by (transition) curves, cants (the vertical distance between the heights of inner and outer edges of railways), and track irregularities on the railway line in the full-scale test are ignored in the simulation. Finally, as explained in Sec. II A 1, windbreaks are properly simplified for the simulation. Based on these, the broad agreement, at least for trends, between the simulation results and test are considered fairly reasonable.

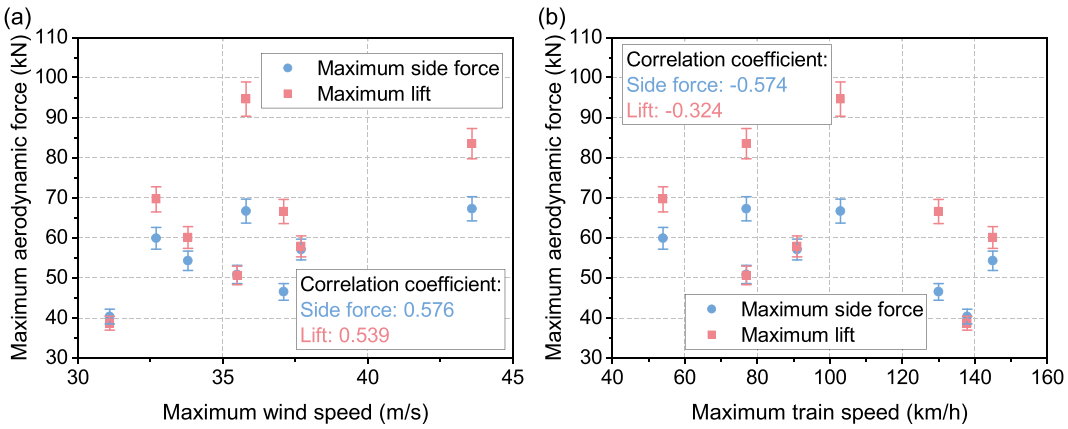

FIG. 12. Maximum aerodynamic forces on leading vehicle at (a) different maximum wind speed and (b) different maximum train speed.

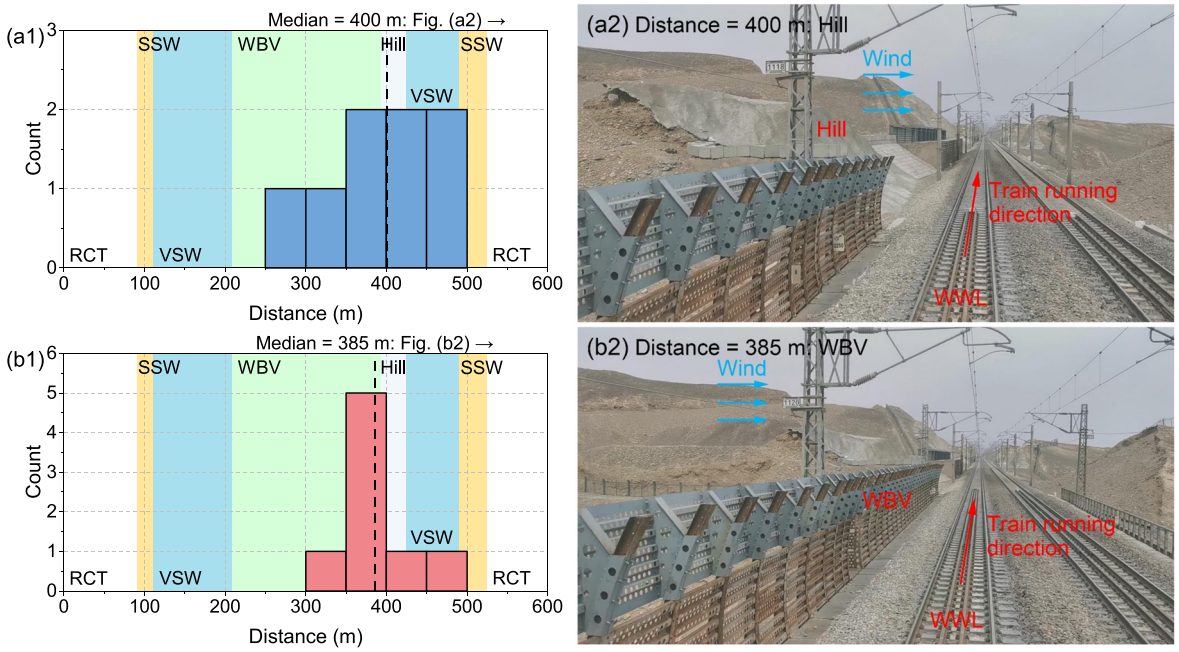

FIG. 13. Locations of (a) maximum side force and (b) maximum lift.

2. Aerodynamic characteristics at different inlet wind speeds

Inlet wind speeds lead to different wind speeds above the railway line and hence the different aerodynamic characteristics of the train passing by the windbreak. Since the leading vehicle is the most cross-wind sensitive,[62] this section analyses the aerodynamic characteristics of the leading vehicle at different wind speeds. Through a comprehensive comparison of the wind speed distributions at different heights above the WWL and LWL in Figs. 8(c) and 8(d), the wind speed above the WWL is generally higher than that above the LWL. Thus, this section focuses on the aerodynamic characteristics of the leading vehicle [see Fig. 2(b)] on the WWL, which is consistent with what happens on Southern Xinjiang Railway.

Figure 15 presents the side force, lift, and rolling moment on the leading vehicle on the WWL at different inlet wind speeds and a train speed of 80 km/h, as well as the relationships between the maximum loads and wind speed. It also includes the normalized wind speed (gray curves with right vertical axes) at a height of $0.5H$ above the WWL shown in Fig. 8(d) (at an inlet wind speed of 30 m/s). The aerodynamic loads on the leading vehicle at different inlet wind speeds change, and their values increase with an increase in wind speed. The aerodynamic loads are associated with the wind speed above the line. The aerodynamic loads are often large at those locations subject to high wind speeds. The locations subject to large side force and rolling moment are near the transitions between the SSW and RCT, and between the WBV and VSW, and close to locations subject to high

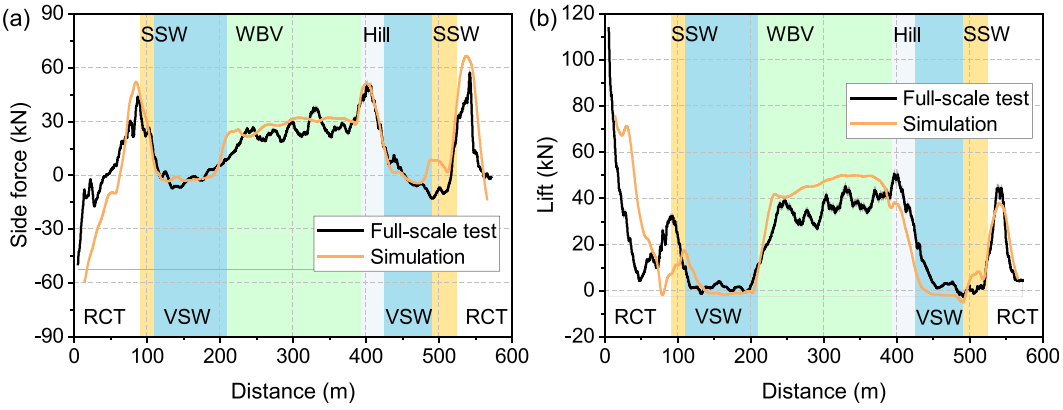

FIG. 14. Aerodynamic forces in numerical simulation and full-scale test based on inlet wind at 35.5 m/s and train speed at 77 km/h: (a) side force and (b) lift.

TABLE II. Differences of the maximum side force and lift (after removing aerodynamic forces in railway cuttings).

Method	Maximum side force	Maximum lift
Numerical simulation	51.517 kN	50.014 kN
Full-scale test	50.840 kN	50.600 kN
Difference	1.3%	−1.2%

wind speeds. The lift force is largest downstream of the WBV, in line with locations of maximum aerodynamic forces from full-scale tests (see Fig. 13). The maximum side force and rolling moment are fairly proportional to inlet wind speed to the power 1.60, and the maximum lift is proportional to the wind speed to the power 1.77. Specifically, the maximum rolling moment increases by 109.2% when inlet wind speed rises from 25 to 40 m/s. The maximum lift can sometimes appear near the distance of zero (the RCT). However, due to the artificial stretching in the topographic model, as discussed in Sec. III B 1, these maxima are disregarded. Additionally, variations in aerodynamic loads are more gradual compared to the wind speed above the line. This is because aerodynamic loads result from wind speeds at various positions along the length of the vehicle and is an integrated quantity. (Theoretically, wind speeds could be processed differently using a moving spatial average based on a window size equal to the vehicle length.[16])

Consistent with these findings, Gao *et al.*[43] measured aerodynamic loads on a leading vehicle at the RCT-SSW transition, observing local load maxima near the transition, similar to the results here. Liu *et al.*[44] also noted local maxima in rolling moment at transitions between VSW and SSW, and SSW and RCT, with significantly higher maxima at the SSW-RCT transition, a pattern that matches the trends in Fig. 15. Their observations of the frequent occurrence of local maxima at windbreak transitions, followed by WBVs, also align with this study's results.

Figure 16 represents the pressure on the windward and leeward sides of the leading vehicle at different inlet wind speeds and the train speed of 80 km/h at the various locations giving rise to the aerodynamic loads as shown in Fig. 15. At the distance of 212.75 m (the transition between the VSW and WBV), as wind speed increases, the

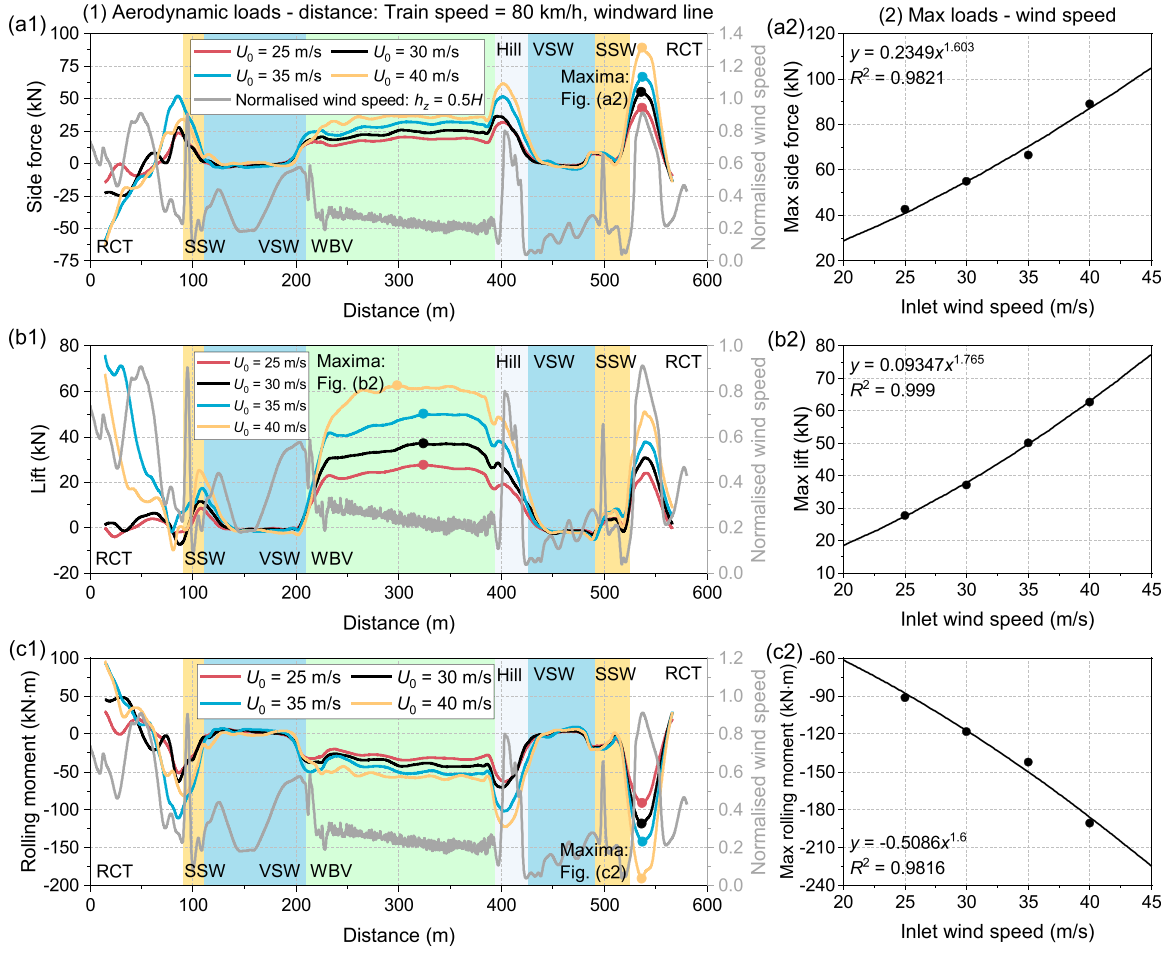

FIG. 15. Aerodynamic loads and their maxima on leading vehicle at different inlet wind speeds: (a) side force, (b) lift, and (c) rolling moment. (Train speed is at 80 km/h.)

pressure coefficient on the windward side of the vehicle rises while it decreases on the leeward side. A high positive pressure is also observed in the middle of the windward side of the vehicle [highlighted in the green box in Fig. 16(a1)], precisely at the transition between the VSW to WBV. The VSW provides a stronger protection than the WBV, causing the flow blocked by the VSW to move longitudinally before entering the range of the railway line from the WBV, consistent with the findings in Sec. III A 3. At the distance of 308.75 m (the WBV), a high negative pressure occurs at the transition between the windward side and the roof of the vehicle. This is due to the continual accelerated flow passing the WBV and creating high negative pressure in this area. Similar phenomena of negative pressure as observed on the first half of the vehicle at the distance of 212.75 m [the blue box in Fig. 16(a1)] and on the second half of leading vehicle at the distance of 404.75 m [the blue box in Fig. 16(a3)] can be found. At the distance of 404.75 m (at the hill), a significant positive pressure is present on the front of the windward side of the vehicle. This results from the low effective height of the windbreak, caused by the upstream hill, which directs the inlet wind onto the windward side of the vehicle, as also depicted in Fig. 9(b3).

To help readers better understand the pressure changes on a train's surface, we have provided two videos related to Fig. 16. Figure 16(a) (Multimedia view) demonstrates the surface pressures on the train as it travels through the multiform windbreak with an inlet wind speed of 40 m/s and a train speed of 80 km/h. Figure 16(b) focuses specifically on the leading vehicle.

Figure 17 presents the wind speed distributions and two-dimensional streamlines in the cross section in the middle of the leading vehicle at the inlet wind speed of 30 m/s and the train speed of 80 km/h, which confirm the analysis mentioned earlier for the positive and negative pressures on the vehicle surface in Fig. 16. By comparing Fig. 17 with Fig. 9(b), it is evident that the vehicle has a rather minor effect on the upstream flow under consideration. This observation suggests the possibility and great potential to estimate the aerodynamic loads on the vehicle just using the upstream wind speed above the railway line (see Sec. III C).

3. Aerodynamic characteristics at different train speeds

Different train speeds usually lead to different aerodynamic characteristics of the train in identical wind conditions above the railway line. This section analyzes the aerodynamic characteristics of the leading vehicle at different train speeds.

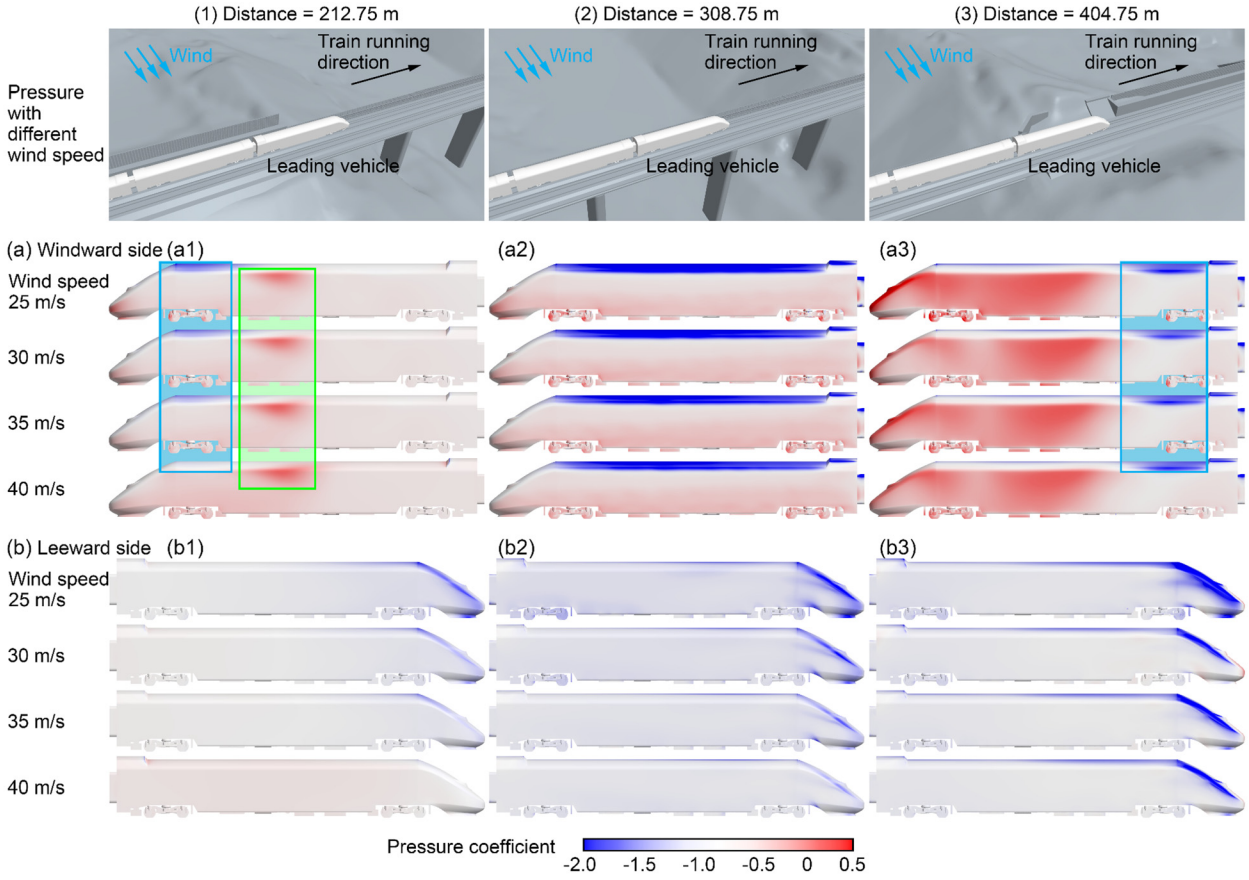

FIG. 16. Pressure on surface of leading vehicle at different locations along railway line at different inlet wind speeds and train speed at 80 km/h: (a) windward side and (b) leeward side. Multimedia available online.

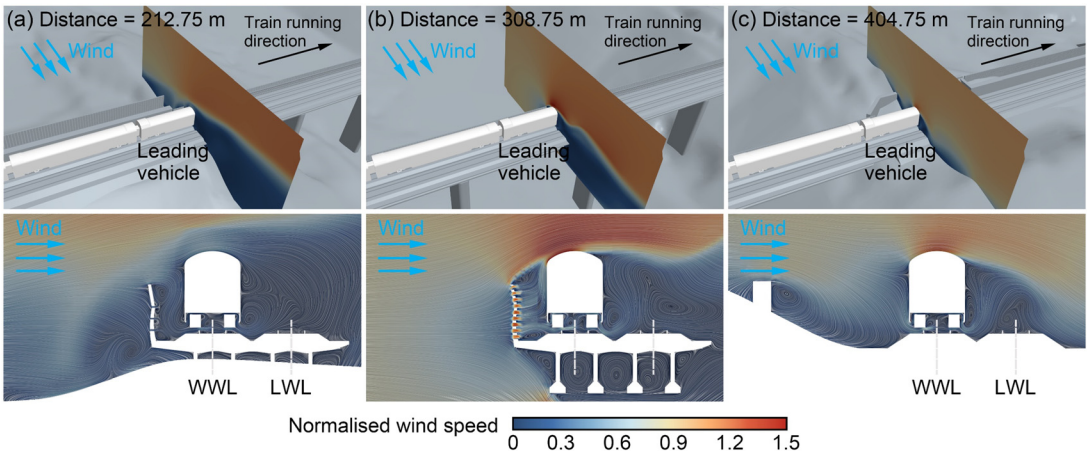

FIG. 17. Normalized wind speeds and streamlines around leading vehicle at different locations along railway line at distances of: (a) 212.75, (b) 308.75, and (c) 404.75 m. (Inlet wind speed is at 30 m/s and train speed is at 80 km/h.)

Figure 18 presents the side force, lift, and rolling moment on the leading vehicle on the WWL at different train speeds and an inlet wind speed of 30 m/s, as well as the relationships between the maximum loads and train speed, where v_{tr} is the train speed. Like Fig. 15, it includes the normalized wind speed (gray curves with right vertical axes) at the height of 0.5H above the WWL in Fig. 8(d). The aerodynamic loads on the leading vehicle exhibit consistent patterns at different train speeds, with their values increasing as train speed increases. This implies that reducing train speed can enhance crosswind safety of railway operations. The locations subject to the high aerodynamic loads remain essentially the same as those identified in Fig. 15. The maximum side force, lift, and rolling moment are proportional to the 0.51st, 0.21st, and 0.48th power of train speed, respectively. The maximum rolling moment increases by 66.0% when train speed rises from 60 to 160 km/h. These findings support the inference from Sec. III B 1 that aerodynamic loads correlate positively with train speed, although train speed has a lesser impact on aerodynamic loads compared to inlet wind speed.

Figure 19 represents the pressure on the windward and leeward sides of the leading vehicle at different train speeds and the inlet wind speed of 30 m/s at the mentioned locations. The train speed primarily affects the pressure on the streamlined head of the vehicle (highlighted in the green box in Fig. 19). As train speed increases, the pressures on both the windward and leeward sides of the streamlined head also increase, likely due to the impact of the longitudinal flow relative to the train. At the distance of 212.75 m (the transition between the VSW and WBV), the variation in pressure on the streamlined head is less pronounced than that at other locations along the railway line [see Fig. 19(a1)]. Additionally, train speed influences the pressure on the surface of the air conditioning unit on the roof (highlighted in the blue box in Fig. 19). Negative pressures on both the windward and leeward sides of the air conditioning unit increase with the increasing of the train speed.

Figure 20 shows the wind speed distributions and two-dimensional streamlines in four cross sections (evenly distributed along the length of the leading vehicle) at different train speeds and an inlet wind speed of 30 m/s. For lack of space, only the cases of the train speeds of 60 and 160 km/h are shown here. At the distance of 212.75 m (the transition between the VSW and WBV), a vortex forms around the transition between the leeward side and the bottom of the vehicle (and indicated nominally by V1 in the figure). This vortex, likely created by flow exiting from bottom of the vehicle, is small and unaffected by train speed. It appears to stem from the intensified flow caused by the windbreak transition, which train speed does not significantly impact. This flow around the leeward side of the vehicle results in low pressure that is mostly independent of train speed. At the distances of 308.75 m (the WBV) and 404.75 m (the hill), two vortices indicated nominally by V1 and V2, form around the leeward side of the vehicle. Vortex V2, originating near the top of the vehicle, grows in size along its length and moves further away from the vehicle as it develops. In contrast, vortex V1, which forms near the bottom, stays close to the vehicle and expands only slightly. The movement paths of vortices V1 and V2 change with train speed, but the overall trends remain fairly consistent. At these two locations, the vehicle is directly affected by the inlet wind, causing the flows around its leeward side to share some similarities with those observed in previous simulations without windbreaks.[63,64]

Among these locations giving rise to large aerodynamic loads, the distance of 404.75 m (the hill) is the most dangerous [as explained by the wind speed distributions in shown Fig. 9(c)]. The three-dimensional flow structures around the train are analyzed at this location (the two-dimensional flow structures only allow one to understand the discrete flow around the train). Figure 21 represents the vorticity and turbulent kinetic energy on the horizontal plane at 0.5H around the train at different train speeds and the inlet wind speed of 30 m/s, and a second-generation identifying method of vortices, Q-method, is used to identify the vortices ($Q = 400\ s^{-2}$).[33,65–67] The vorticity and turbulent kinetic energy around the leeward side of the leading vehicle are substantial and generally increase with an increase in train speed. The vortices in this region are generated by the streamlined head and the transition between the leeward side and roof.[68,69] These vortices move toward the tail of the train and gradually away from it. As train speed increases, the vortices approach the train, similar to the effect of yaw angle on vortices around the leeward side of a

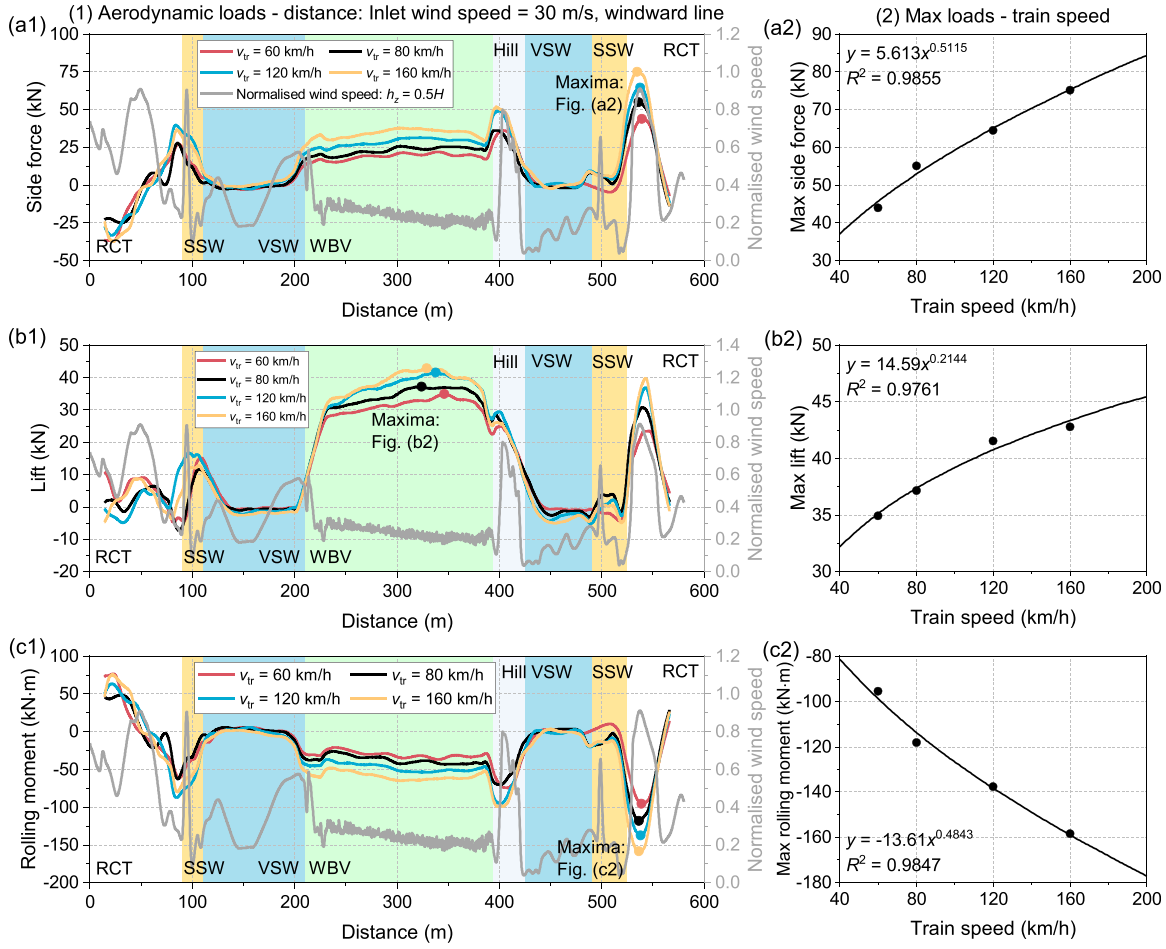

FIG. 18. Aerodynamic loads and their maxima on leading vehicle at different train speeds: (a) side force, (b) lift, and (c) rolling moment. (Inlet wind speed is at 30 m/s.)

vehicle.[70] This phenomenon also explains the gradual increase in negative pressure on the leeward side with increasing train speed, as shown in Figs. 19(b2) and 19(b3).

C. Exploration of simplified calculation for aerodynamic loads

The engineering purpose of the numerical simulations on the aerodynamic characteristics of the train passing by the multiform windbreak in complex terrains is to assess the crosswind stability of the vehicle, that is, to calculate the characteristic wind curves (CWCs). For the CWC calculation, at least 12 combinations of wind speeds and train speeds (often more than 12) should be simulated, and at least 214 272 core hours was consumed in this work (see Sec. II A 4). It would expend many computational resources and needs to be simplified. According to Sec. III B 2, the aerodynamic loads on the vehicle passing by the multiform windbreak and the wind speed above the railway line are highly correlated. The main aim of the section is to explore a simplified calculation method for the aerodynamic loads on the vehicle based on the wind speed distribution above the line.

The flow downstream of the windbreak is complex, and it is very difficult for the wind speeds at the two heights in Figs. 8(c) and 8(d) to reflect the overall performance across the wind speed above the railway line, as we have discussed in Sec. III A 2. On the x-z plane on the centerline of the WWL [see Fig. 22(a)], Fig. 22(b) represents the longitudinal wind speed at the height above the top of the rail of no more than H (= 4.433 m) at the inlet wind speed of 30 m/s (in the absence of the moving train). The longitudinal wind speed vector is pointing in the direction of the positive axis x in Fig. 6. The areas experiencing high longitudinal wind speeds above the WWL are located near the transitions between the windbreaks.

Figure 22(c) presents the wind pressure associated with the wind speed in the y direction at the height above the top of the rail of no more than H on the x-z plane on the centerline of the WWL at the inlet wind speed of 30 m/s. The wind pressure w_p is calculated from the following

$$w_p = \frac{\rho U_y^2}{2}, \tag{3}$$

where U_y is the wind speed in the y direction. As shown in Fig. 8(c), the areas experiencing high y-wind speeds are situated downstream of the

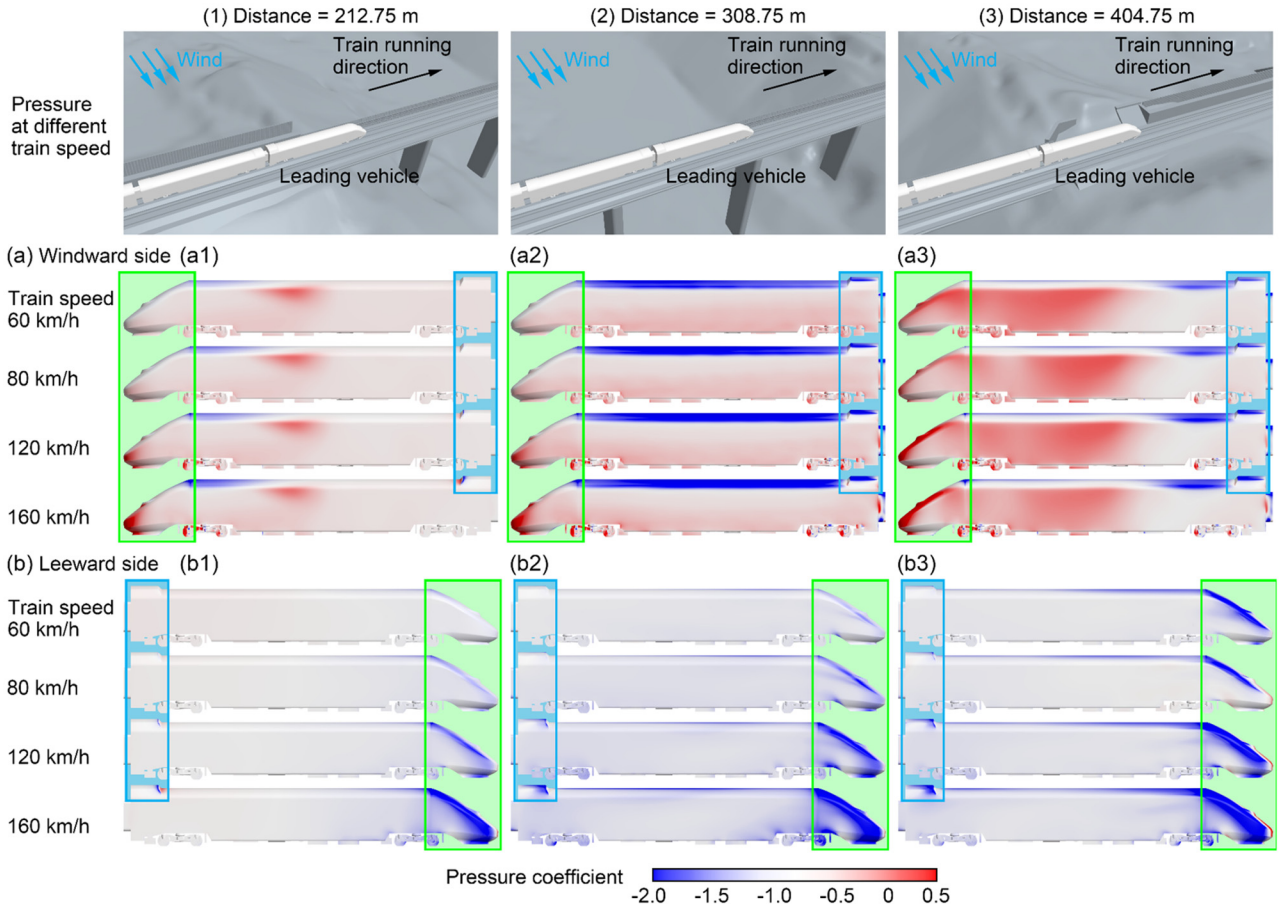

FIG. 19. Pressure on surface of leading vehicle at different locations along railway line at different train speeds: (a) windward side and (b) leeward side. (Inlet wind speed is at 30 m/s.)

WBV and at the transitions between the windbreaks. Observing the aerodynamic loads on the leading vehicle in Fig. 15, it is clear that the aerodynamic loads are more strongly correlated with the y-wind speed than with the longitudinal wind speed, which aligns with expectations.

Figure 23 defines/emphasizes the wind load and the side force.

- **Wind load (without a train):** Wind speeds at different positions of the vehicle surface are different, as Sec. III B 2 illustrates. Assuming a window whose size equal to the length of the leading vehicle (28.5 m) moves in the train running direction in Fig. 22(c), and the wind pressures in it are added up as vectors depending on the direction of the local y-wind speeds (in the absence of the moving train). The sum is the wind load F_D,

$$F_D = \int\int_S \frac{U_y}{|U_y|} w_p \mathrm{d}x\mathrm{d}z. \tag{4}$$

- **Side force (with a moving train):** The side force here is the aerodynamic force in the y direction on the leading vehicle.

Figure 24(a) presents the wind load (with the left axis) and the side force on the leading vehicle in Fig. 15(a) (with the right vertical axis). The wind load and side force exhibit the same trend, although their absolute values differ. The correlation coefficient between them is 0.939.

Figure 24(b) illustrates the ratio of the side force to wind load, where outliers have been removed according to the median absolute deviations downstream of different windbreaks. The ratio of side force to wind load remains largely constant downstream of a single windbreak but fluctuates at the transitions between windbreaks, specifically within half the length of the leading vehicle before and after these transitions. The mean ratios downstream of different windbreaks (excluding the regions within half the length of the leading vehicle before and after the windbreak transitions) are shown in the bar graph, with error bars representing standard deviations. The mean ratio for the distances in the 90.846–110.757 m range (the SSW) is not calculated due to the wall length being shorter than vehicle length. For each type of windbreak, the ratios are generally stable, except for the RCT. The ratios downstream of the two VSWs are similar, with only a 4.2% difference between them. Large standard deviations are observed downstream of the VSWs and attributed to the near-zero values of wind load and side force. The ratio does not directly reflect the protection performance of the windbreak, which is mostly associated with the flow structures

FIG. 20. Normalized wind speeds and streamlines around leading vehicle at different locations along railway line at different train speeds of: (a) 60 and (b) 160 km/h. (Inlet wind speed is at 30 m/s.)

downstream of the windbreak and the longitudinal velocity above the railway line.

The aerodynamic loads on the vehicle can be simplified and calculated based on the mean ratios described above and numerical simulations of wind speed (or wind pressure) above the railway line. This work presents ratios based on limited simulations and aims to explore the feasibility of this simplified method. Furthermore, research should involve extensive simulations and wind tunnel tests to obtain

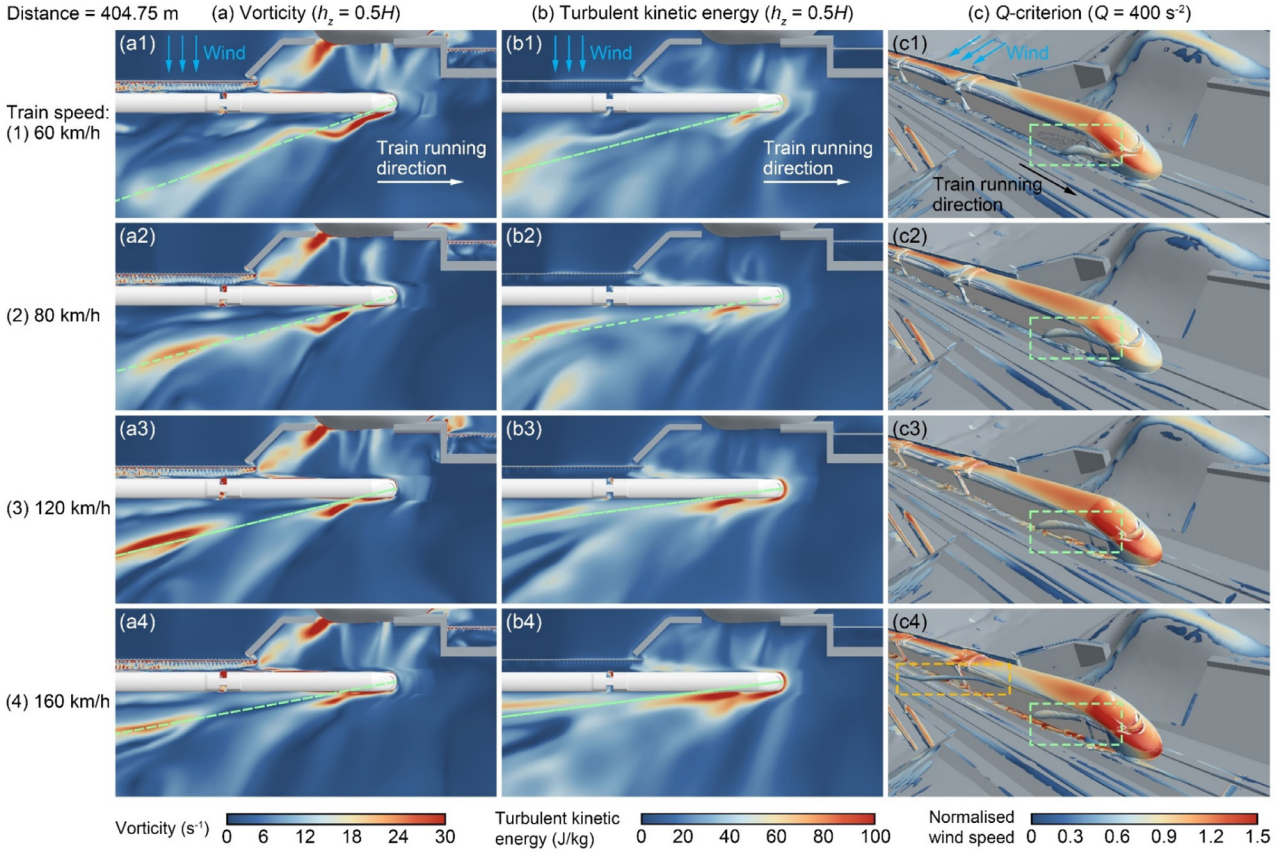

FIG. 21. Flow structures around train at distance of 404.75 m at different train speeds: (a) vorticity, (b) turbulent kinetic energy, and (c) Q-criterion ($Q = 400\ s^{-2}$). (Inlet wind speed is at 30 m/s.)

these ratios more comprehensively. Ultimately, a database could be developed, including ratios for various configurations such as topography, windbreaks, infrastructures, and trains, to enhance the accuracy and adaptability of this simplified approach. This will be the focus of our future work.

The side force on the vehicle is simplified and calculated based on the wind load and mean ratios in Fig. 24. Figure 25 illustrates this simplified side force and the simulated side force on the leading vehicle in Fig. 15(a), as well as the ratio of the side force to wind load here (the gray curves with the right vertical axes). The ratios downstream of the transitions between windbreaks (within half the length of the leading vehicle before and after the transitions) are processed using interpolation calculations. The simplified side force can generally reflect the change in the simulated side force downstream of the windbreaks, except for the RCT at the distance less than 90.846 m. The error of the maximum side force is 8.4%. As the accuracy and adaptability of the side force to wind load ratio are improve in future work, this error is expected to be further reduced.

Once an accurate and comprehensive database of aerodynamic load to wind load ratios is established, it will only be necessary to simulate wind speeds above the railway line for various inlet wind speeds, rather than simulating aerodynamic characteristics of the train at different inlet wind speeds and train speeds. This approach will significantly conserve computational resources. Although building the database requires substantial computational effort, it provides a long-term solution. For this study, the individual wind speed simulation and aerodynamic load simulation consume 4224 core hours and 15 744 core hours, respectively, as described in Sec. II A 4. Considering 12 combinations of wind speeds and train speeds (the optimal condition previously discussed) for calculating the CWC, Table III compares the computational resources required for the simplified and original methods. The simplified method achieves an 88.2% reduction in computational resources, with even greater savings when accounting for simulation preparation. Additionally, since normalized wind speed shows minimal variation with inlet wind speed [as shown in Figs. 8(a) and 8(b)], further reductions in computation are anticipated.

IV. CONCLUSIONS AND OUTLOOKS

In this work, the flow downstream of the multiform windbreak and the aerodynamic characteristics of the train passing by the windbreak are simulated in complex terrains. The protection performance of the multiform windbreak is evaluated, and the effects of inlet wind speed and train speed on aerodynamic characteristics of the vehicle are analyzed. A simplified method for calculating aerodynamic loads on the vehicle based on wind speed distribution above the railway line is also explored. The main conclusions are as follows:

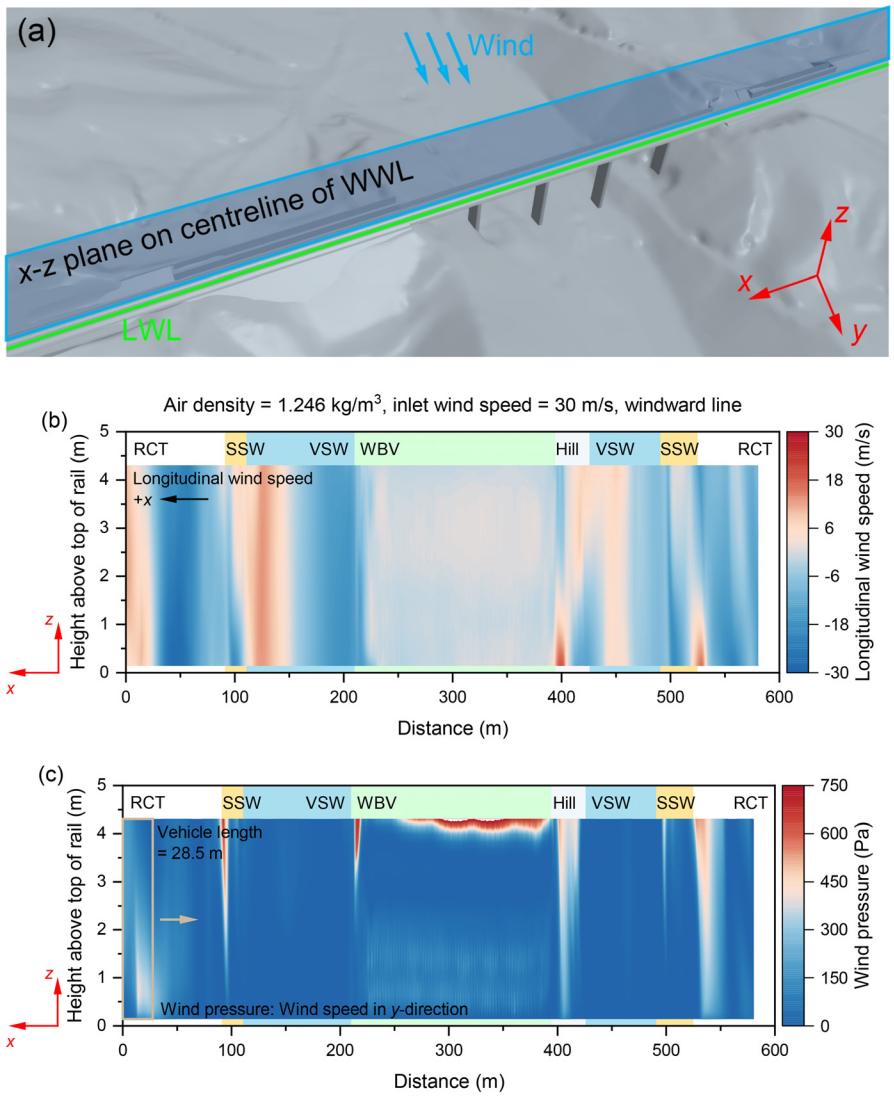

FIG. 22. (a) *x*–*z* plane on centerline of windward line, (b) longitudinal wind speed, and (c) lateral wind pressure (w_p) above windward line.

(1) The protection performance of different windbreaks in the multiform windbreak varies. This performance can be characterized by the wind speed (distribution) above the railway line or the air pressure around the windbreak. The ability of a windbreak to raise the inlet wind, which depends on its aerodynamic configuration and effective height, dictates its wind-protection performance. The performance of the RCT is related to its height, while the VSW (with an upstream wind barrier) outperforms both the SSW and the WBV. The SSW provides better protection for the WWL compared to the

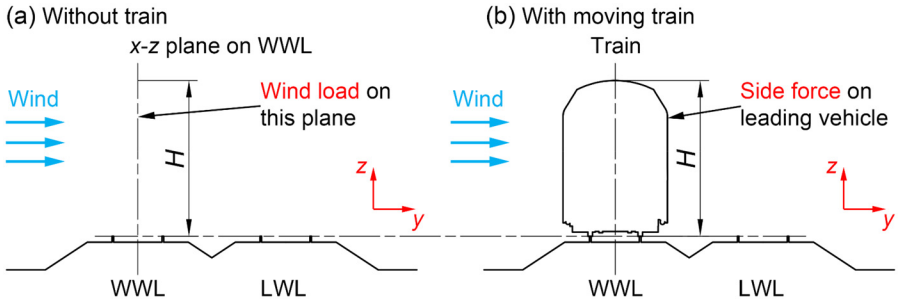

FIG. 23. Schematic of (a) wind load without train and (b) side force with moving train.

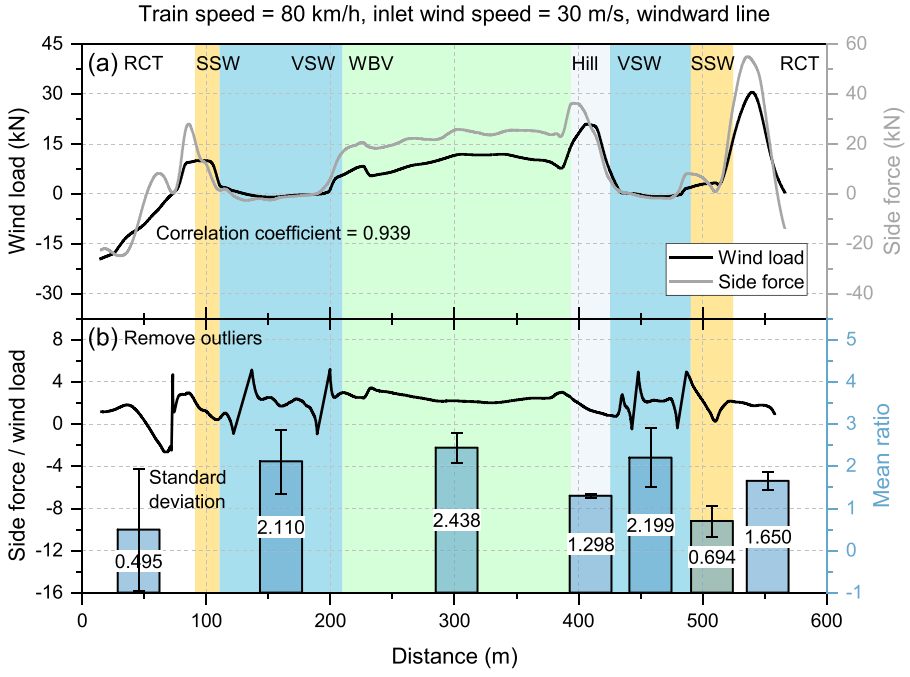

FIG. 24. (a) Wind load (F_D) and (b) ratio of side force to wind load and its means.

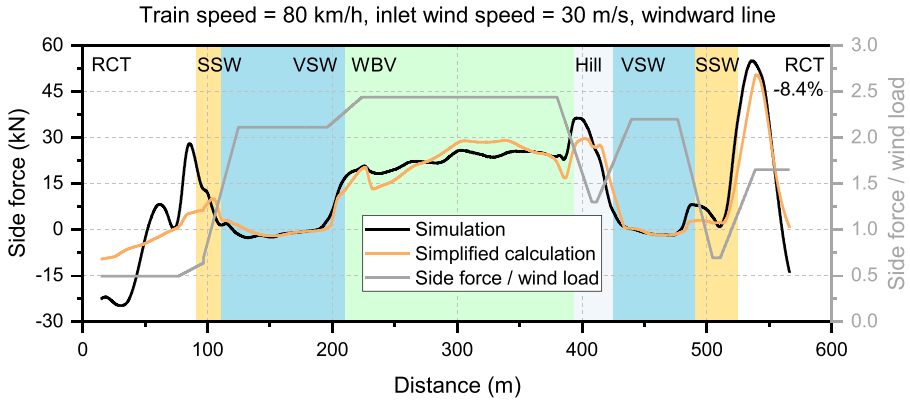

FIG. 25. Simplified side force and simulated side force on leading vehicle.

LWL, whereas the WBV offers stronger protection for the LWL.

(2) Areas with high wind speeds above the railway line are primarily located downstream of the transitions between windbreaks, typically near to the windbreak with weaker protection performance. The flow upstream of the windbreaks moves longitudinally from the stronger windbreak to the weaker one, accumulating and entering the range of the line near the weaker windbreak. For a railway line that require the construction or modification of a multiform windbreak due to terrain, it is recommended to use windbreaks with similar protection performances. Neighboring windbreaks should have nearly equal performance to avoid weak transition areas. Improving the performance of an individual windbreak is minimally effective and may even reduce the performance of the adjacent transition areas.

(3) The aerodynamic characteristics of the train passing by the multiform windbreak in complex terrains are influenced by both the inlet wind speed and the train speed. The maximum side force and rolling moment on the leading vehicle are proportional to the wind speed to the power 1.6 and to the train

TABLE III. Computational resources required in original and simplified methods.

Method	Simulated cases	Computational resources (core hours)
Original method	6 wind speed simulations and 12 aerodynamic load simulations	214 272
Simplified method	6 wind speed simulations	25 344
Difference	...	−88.2%

speed to the power 0.5. While the wind speed does not alter the basic flow pattern around the vehicle, it does affect the magnitude of aerodynamic quantities. The train speed primarily impacts the pressure distribution on the streamlined head of the vehicle and the vortices around the leeward side. As train speed increases, the pressure on the streamlined head rises, and the vortices move closer to the train.

(4) The aerodynamic loads on the vehicle are highly correlated with the wind speed above the railway line. A simplified method for calculating these loads based on the wind speed distribution above the line is proposed, with an error margin of 8.4% for the maximum side force. This simplified method can save at least 88.2% of computational resources when assessing the crosswind stability of a vehicle passing by the multiform windbreak in complex terrains. For assessing the crosswind safety of railway operations, evaluation of aerodynamic loads is the most time-consuming course in the process, and therefore, this accurate and effective method has significant engineering implications.

This work serves as an initial step in exploring the simplified method for evaluating aerodynamic loads based on wind speed distribution, which aims to assess its feasibility. Its accuracy and adaptability will be enhanced in the next stage of our research. Specifically, the ratio of aerodynamic load to wind load [see Fig. 24(b)] will be evaluated through numerical simulations and wind tunnel tests. We will create a database of these ratios for various configurations, including different topographies, windbreaks, infrastructures, and trains. Additionally, based on recent studies on the effects of turbulent inlet wind on the aerodynamic and dynamic characteristics of vehicles,[63,71–73] we will incorporate turbulent inlet wind in future simulations. These simulations will be based on locally measured fluctuating characteristics of wind to study the impacts of inlet and local turbulence on the crosswind stability of vehicles downstream of windbreaks.

ACKNOWLEDGMENTS

This work was supported by the China National Railway Group Science and Technology Program (Grant No. N2023T010), the Science and Technology Innovation Program of Hunan Province, China (Grant No. 2022RC3040), the Natural Science Foundation of Hunan Province, China (Grant No. 2022JJ30727), the Technology Research and Development Program of China Railway Urumqi Group Co., Ltd. (Grant No. 2023-kj-48), China Scholarship Council (Grant No. 202206370140), and Fundamental Research Funds for the Central Universities of Central South University (Grant No. 2022ZZTS0630). This work was carried out in part using computing resources at the High Performance Computing Center of Central South University. The authors are grateful to Mr. Zhanhao Guo at the Hong Kong Polytechnic University for help on the topographic model.

AUTHOR DECLARATIONS

Conflict of Interest

The authors have no conflicts to disclose.

Author Contributions

Hongrui Gao: Conceptualization (lead); Formal analysis (lead); Methodology (equal); Writing – original draft (lead). **Tanghong Liu:** Project administration (lead); Writing – review & editing (supporting). **Xiaodong Chen:** Supervision (equal); Writing – review & editing (equal). **Haoyang Zeng:** Investigation (equal). **Guang Chen:** Software (equal). **Zheng-Wei Chen:** Supervision (supporting). **Jie Zhang:** Writing – review & editing (supporting). **Boo Cheong Khoo:** Supervision (lead); Writing – review & editing (lead).

DATA AVAILABILITY

The data that support the findings of this study are available from the corresponding author upon reasonable request and with the permission of China Railway Urumqi Group Co., Ltd.

REFERENCES

[1]X. Tian, H. Xiang, X. Chen, and Y. Li, "Dynamic response analysis of high-speed maglev train-guideway system under crosswinds," J. Cent. South Univ. **30**(8), 2757–2771 (2023).
[2]R. G. Gawthorpe, "Wind effects on ground transportation," J. Wind Eng. Ind. Aerodyn. **52**, 73–92 (1994).
[3]T. Imai, T. Fujii, K. Tanemoto, T. Shimamura, T. Maeda, H. Ishida, and Y. Hibino, "New train regulation method based on wind direction and velocity of natural wind against strong winds," J. Wind Eng. Ind. Aerodyn. **90**(12–15), 1601–1610 (2002).
[4]H. Liu, H. Tian, and Y. Li, "An EMD-recursive ARIMA method to predict wind speed for railway strong wind warning system," J. Wind Eng. Ind. Aerodyn. **141**, 27–38 (2015).
[5]C. Wetzel and C. Proppe, "On reliability and sensitivity methods for vehicle systems under stochastic crosswind loads," Veh. Syst. Dyn. **48**(1), 79–95 (2010).
[6]T. Zhang, H. Xia, and W. W. Guo, "Analysis on running safety of train on bridge with wind barriers subjected to cross wind," Wind Struct. **17**(2), 203–225 (2013).
[7]R. Chen, Q. Zeng, Y. Huang, J. Xiang, Y. Wen, X. Guo, C. Yin, H. Dong, and G. Zhao, "Analysis theory of random energy of train derailment in wind," Sci. China Phys. Mech. Astron. **53**(4), 751–757 (2010).
[8]X.-Z. Li, J. Xiao, D.-J. Liu, M. Wang, and D.-Y. Zhang, "An analytical model for the fluctuating wind velocity spectra of a moving vehicle," J. Wind Eng. Ind. Aerodyn. **164**, 34–43 (2017).
[9]T. Liu, L. Wang, H. Gao, Y. Xia, Z. Guo, W. Li, and H. Liu, "Research progress on train operation safety in Xinjiang railway under wind environment," Transp. Saf. Environ. **4**(2), tdac005 (2022).
[10]W. Guo, H. Xia, R. Karoumi, T. Zhang, and X. Li, "Aerodynamic effect of wind barriers and running safety of trains on high-speed railway bridges under cross winds," Wind Struct. **20**(2), 213–236 (2015).
[11]B. Li, S. Feng, Q. Yang, and Y. Hou, "Researches and application of railway wind-break wall," in *Advanced Engineering Materials, Pts 1–3*, edited by J. M. Zeng, T. S. Li, S. J. Ma, Z. Y. Jiang, and D. G. Yang (Trans Tech Publications Ltd, Stafa-Zurich, 2011), pp. 1126–1129.
[12]M. Mohebbi and M. A. Rezvani, "Two-dimensional analysis of the influence of windbreaks on airflow over a high-speed train under crosswind using lattice Boltzmann method," Proc. Inst. Mech. Eng., Part F **232**(3), 863–872 (2018).
[13]H. Gu, T. Liu, Z. Jiang, and Z. Guo, "Research on the wind -sheltering performance of different forms of corrugated wind barriers on railway bridges," J. Wind Eng. Ind. Aerodyn. **201**, 104166 (2020).
[14]J. Zhang, K. He, J. Wang, T. Liu, X. Liang, and G. Gao, "Numerical simulation of flow around a high-speed train subjected to different windbreak walls and yaw angles," J. Appl. Fluid Mech. **12**(4), 1137–1149 (2019).
[15]S. Avila-Sanchez, O. Lopez-Garcia, A. Cuerva, and J. Meseguer, "Characterisation of cross-flow above a railway bridge equipped with solid windbreaks," Eng. Struct. **126**, 133–146 (2016).
[16]European Committee for Standardization (CEN), *Railway applications - Aerodynamics Part 6: Requirements and test procedures for cross wind assessment* (European Committee for Standardization, 2022).

[17]G. Tomasini, S. Giappino, F. Cheli, and P. Schito, "Windbreaks for railway lines: Wind tunnel experimental tests," Proc. Inst. Mech. Eng., Part F **230**(4), 1270–1282 (2016).
[18]E. Deng, H. Yue, Y.-Q. Ni, X.-H. He, W.-C. Yang, and Z.-W. Chen, "Wake dynamic characteristics of windproof structures in embankment-bridge sections along a high-speed railway under natural strong crosswinds," Phys. Fluids **35**(5), 055109 (2023).
[19]T. Liu, Z. Chen, X. Zhou, and J. Zhang, "A CFD analysis of the aerodynamics of a high-speed train passing through a windbreak transition under crosswind," Eng. Appl. Comput. Fluid Mech. **12**(1), 137–151 (2018).
[20]T. Liu and J. Zhang, "Effect of landform on aerodynamic performance of high-speed trains in cutting under cross wind," J. Cent. South Univ. **20**(3), 830–836 (2013).
[21]Y. Xia, T. Liu, X. Su, Z. Jiang, Z. Chen, and Z. Guo, "Aerodynamic influences of typical windbreak wall types on a high-speed train under crosswinds," J. Wind Eng. Ind. Aerodyn. **231**, 105203 (2022).
[22]F. Yang, T. Liu, Z. Shi, Y. Xia, Z. Jiang, and T. Han, "Influence of height of earth embankment type windbreak wall on flow field characteristics and catenary wind-induced displacement," Eng. Appl. Comput. Fluid Mech. **15**(1), 672–691 (2021).
[23]J. Zhang, G. Gao, T. Liu, and Z. Li, "Shape optimization of a kind of Earth embankment type windbreak wall along the Lanzhou-Xinjiang Railway," J. Appl. Fluid Mech. **10**(4), 1189–1200 (2017).
[24]X. Wang, T. Liu, Y. Xia, H. Gao, X. Huo, B. Xu, and Z. Chen, "Effect of railway cutting depths on running safety and pantograph–catenary interaction of trains under crosswind," J. Wind Eng. Ind. Aerodyn. **245**, 105659 (2024).
[25]J. Zhang, G. Gao, T. Liu, and Z. Li, "Crosswind stability of high-speed trains in special cuts," J. Cent. South Univ. **22**(7), 2849–2856 (2015).
[26]X. Dong, T. Liu, Y. Xia, F. Yang, Z. Chen, and Z. Guo, "Comparative analysis of the aerodynamic performance of trains and dynamic responses of catenaries for windbreak walls with different heights under crosswind," Proc. Inst. Mech. Eng., Part F **237**(3), 335–346 (2023).
[27]E. Brambilla, S. Giappino, and G. Tomasini, "Wind tunnel tests on railway vehicles in the presence of windbreaks: Influence of flow and geometric parameters on aerodynamic coefficients," J. Wind Eng. Ind. Aerodyn. **220**, 104838 (2022).
[28]S. Cheng, T. Liu, W. Li, Z. Liu, and Z. Chen, "Numerical study on reasonable lengths of wind barriers with different thicknesses in wind tunnel tests," J. Cent. South Univ. **30**(4), 1388–1404 (2023).
[29]H. Gu, T. Liu, H. Gao, Z. Liu, and S. Cheng, "Wind tunnel testing on the aerodynamic effect on a train with single-sided and double-sided wind barriers of different lengths," Proc. Inst. Mech. Eng., Part F **237**(3), 394–406 (2023).
[30]H. Gu, H. Gao, T. Liu, S. Cheng, J. Li, and Z. Liu, "Effects of windbreak wall model lengths on aerodynamic characteristics of trains on different tracks in wind tunnel tests—A measurement strategy," J. Wind Eng. Ind. Aerodyn. **228**, 105104 (2022).
[31]S. A. Hashmi, H. Hemida, and D. Soper, "Wind tunnel testing on a train model subjected to crosswinds with different windbreak walls," J. Wind Eng. Ind. Aerodyn. **195**, 104013 (2019).
[32]J. Niu, Y. Zhang, R. Li, Z. Chen, H. Yao, and Y. Wang, "Aerodynamic simulation of effects of one- and two-side windbreak walls on a moving train running on a double track railway line subjected to strong crosswind," J. Wind Eng. Ind. Aerodyn. **221**, 104912 (2022).
[33]Z. Liu, T. Liu, H. Gao, H. Gu, Y. Xia, and B. Xu, "Flow characteristics and wind-sheltering performance of wind barriers with different diameters of holes on railway viaducts," Int. J. Numer. Methods Heat Fluid Flow **33**(11), 3748–3769 (2023).
[34]M. Mohebbi and M. A. Rezvani, "Analysis of the effects of lateral wind on a high speed train on a double routed railway track with porous shelters," J. Wind Eng. Ind. Aerodyn. **184**, 116–127 (2019).
[35]Z. Chen, T. Liu, W. Li, Z. Guo, and Y. Xia, "Aerodynamic performance and dynamic behaviors of a train passing through an elongated hillock region beside a windbreak under crosswinds and corresponding flow mitigation measures," J. Wind Eng. Ind. Aerodyn. **208**, 104434 (2021).
[36]Z. Chen and Y. Ni, "Sudden flow induced by mountain ridges beside windbreaks in a railway and its mitigation measures," Transp. Saf. Environ. **4**(1), tdac004 (2022).
[37]D. Liu, G. M. Tomasini, D. Rocchi, F. Cheli, Z. Lu, and M. Zhong, "Correlation of car-body vibration and train overturning under strong wind conditions," Mech. Syst. Signal Proc. **142**, 106743 (2020).
[38]L.-B. Tang, X.-H. He, L. Yan, and Z. Lin, "Experimental study of aerodynamic characteristics of high-speed train on bridge-tunnel junctions under crosswinds," J. Cent. South Univ. **30**(2), 613–624 (2023).
[39]D. Zhang, M. Zhong, G. Hu, and Y. Xiao, "Numerical study of the unsteady crosswind response of high-speed train under local structure-induced unsteady winds by MBS," Eng. Struct. **281**, 115788 (2023).
[40]M. Gallagher, J. Morden, C. Baker, D. Soper, A. Quinn, H. Hemida, and M. Sterling, "Trains in crosswinds - Comparison of full-scale on-train measurements, physical model tests and CFD calculations," J. Wind Eng. Ind. Aerodyn. **175**, 428–444 (2018).
[41]M. Mohebbi and M. A. Rezvani, "Multi objective optimization of aerodynamic design of high speed railway windbreaks using Lattice Boltzmann Method and wind tunnel test results," Int. J. Rail Transp. **6**(3), 183–201 (2018).
[42]B. Sun, G. Chen, J. Chen, X. Li, M. Tang, and M. Zhong, "Performance of a vehicle-mounted anemometer under crosswind: Simulation and experiment," Transp. Saf. Environ. **5**(3), tdac053 (2023).
[43]H. Gao, T. Liu, H. Gu, Z. Jiang, X. Huo, Y. Xia, and Z. Chen, "Full-scale tests of unsteady aerodynamic loads and pressure distribution on fast trains in crosswinds," Measurement **186**, 110152 (2021).
[44]T.-H. Liu, L. Wang, Z.-W. Chen, H.-R. Gao, W.-H. Li, Z. Guo, Y.-T. Xia, X.-S. Huo, and Y.-W. Wang, "Study on the pressure pipe length in train aerodynamic tests and its applications in crosswinds," J. Wind Eng. Ind. Aerodyn. **220**, 104880 (2022).
[45]L. Wei, J. Zeng, H. Gao, and S. Qu, "On-board measurement of aerodynamic loads for high-speed trains negotiating transitions in windbreak walls," J. Wind Eng. Ind. Aerodyn. **222**, 104923 (2022).
[46]Z. Sun, S. A. Hashmi, H. Dai, X. Cheng, T. Zhang, and Z. Chen, "Safety comparisons of a high-speed train's head and tail passing by a windbreak breach," Veh. Syst. Dyn. **59**(6), 823–840 (2021).
[47]D. Liu, X. Liang, W. Zhou, L. Zhang, Z. Lu, and M. Zhong, "Contributions of bogie aerodynamic loads to the crosswind safety of a high-speed train," J. Wind Eng. Ind. Aerodyn. **228**, 105082 (2022).
[48]X. Xu, C. Li, S. Zhuge, Z. Zhao, X. Yang, B. C. Khoo, S. Srigrarom, B. Lin, and X. Zhang, "A buddy temporal-spatial calibration method for airborne sensors in multi-UAV systems," IEEE Rob. Autom. Lett. **9**(8), 7365–7372 (2024).
[49]Standardization Administration of the People's Republic of China, "Specifications for aerophotogrammetric office operation of 1:500 1:1000 1:2000 topographic maps," Standard No. GB 7930-1987, 2008.
[50]H. Gao, T. Liu, H. Gu, and H. Zeng, "Effects of rail models on aerodynamic characteristics of trains in crosswinds at a large yaw angle," Mech. Based Des. Struct. Mech. (published online) (2024).
[51]Siemens, *STAR-CCM+ Documentation* (Siemens, 2018).
[52]Z. Chen, T. Liu, M. Li, M. Yu, Z. Lu, and D. Liu, "Dynamic response of railway vehicles under unsteady aerodynamic forces caused by local landforms," Wind Struct. **29**(3), 149–161 (2019).
[53]X.-S. Huo, T.-H. Liu, Z.-W. Chen, W.-H. Li, H.-R. Gao, and B. Xu, "Comparison of RANS, URANS, SAS and IDDES for the prediction of train crosswind characteristics," Wind Struct. **37**(4), 303–314 (2023).
[54]H. Gao, T. Liu, Z. Liu, X. Huo, J. Zhang, X. Wang, and Z. Chen, "Discrete integration for measuring aerodynamic loads on trains in crosswinds – realizable strategies of discretization and discrete integration," Measurement **216**, 112967 (2023).
[55]X. Dong, T. Liu, Z. Shi, Y. Xia, F. Yang, and Z. Chen, "Influence of porosity of reformed earth embankment windbreak wall on flow field and displacement of catenary under crosswinds," J. Wind Eng. Ind. Aerodyn. **214**, 104652 (2021).
[56]H. Gu, T. Liu, Z. Jiang, and Z. Guo, "Experimental and simulation research on the aerodynamic effect on a train with a wind barrier in different lengths," J. Wind Eng. Ind. Aerodyn. **214**, 104644 (2021).
[57]Z. Chen, T. Liu, M. Yu, G. Chen, M. Chen, and Z. Guo, "Experimental and numerical research on wind characteristics affected by actual mountain ridges and windbreaks: A case study of the Lanzhou-Xinjiang high-speed railway," Eng. Appl. Comput. Fluid Mech. **14**(1), 1385–1403 (2020).

[58]J. Wang, X.-Y. Liu, E. Deng, Y.-Q. Ni, P.-W. Chan, W.-C. Yang, and Y.-K. Tan, "Acceleration and Reynolds effects of crosswind flow fields in gorge terrains," Phys. Fluids **35**(8), 085143 (2023).
[59]L. Zhao, E. Deng, W. Yang, Y. Ni, W. Zhao, and L. Luo, "Unraveling the impact of cutting transition section on the aerodynamic loads of high-speed trains: Utilizing the IDDES approach," J. Cent. South Univ. **31**(3), 989–1002 (2024).
[60]C. Baker, "A framework for the consideration of the effects of crosswinds on trains," J. Wind Eng. Ind. Aerodyn. **123**, 130–142 (2013).
[61]R. K. Cooper, "The effect of cross-winds on trains," ASME J. Fluids Eng. **103**(1), 170–178 (1981).
[62]F. Cheli, R. Corradi, D. Rocchi, G. Tomasini, and E. Maestrini, "Wind tunnel tests on train scale models to investigate the effect of infrastructure scenario," J. Wind Eng. Ind. Aerodyn. **98**(6–7), 353–362 (2010).
[63]R.-D. Xue, X.-H. Xiong, X.-B. Li, and G. Chen, "Influence of turbulent incoming flow on aerodynamic behaviors of train at 90 degrees yaw angle," Phys. Fluids **35**(1), 015121 (2023).
[64]J. Zhang, A. Xu, F. Huang, Y. Bai, and T. Liu, "A novel vortex control method for improving anti-overturning performance of a high-speed train with leeward airbag structures under crosswinds," Phys. Fluids **36**(6), 065146 (2024).
[65]X. Chen, S. Zhong, T. Liu, J. Zhang, O. Ozer, and G. Gao, "Experimental study on the synergy of sweeping jets on the afterbody flows of a slanted-base cylinder," Aerosp. Sci. Technol. **148**, 109096 (2024).
[66]J. Jeong and F. Hussain, "On the identification of a vortex," J. Fluid Mech. **285**, 69–94 (1995).
[67]Z. Ren, D. Li, Y. Qin, H. Wang, J. Liu, and Y. Li, "Correlation between hydraulic loss and characteristic vorticities in a mechanical pump," Phys. Fluids **35**(6), 065120 (2023).
[68]F. Cheli, F. Ripamonti, D. Rocchi, and G. Tomasini, "Aerodynamic behaviour investigation of the new EMUV250 train to cross wind," J. Wind Eng. Ind. Aerodyn. **98**(4–5), 189–201 (2010).
[69]J. Zhang, Y. Ding, F. Wang, N. Xiang, A. Xu, Z. Chen, and M. Tang, "Comparison of aerodynamic performance of trains running on bridges under crosswinds using various motion modes," Phys. Fluids **35**(12), 125125 (2023).
[70]R.-D. Xue, X.-H. Xiong, and G. Chen, "Flow dynamics of train under turbulent inflow at different crosswind yaw angles," Phys. Fluids **36**(3), 035176 (2024).
[71]G. Chen, X.-B. Li, K. He, Z. Cheng, D. Zhou, and X.-F. Liang, "Effect of the free-stream turbulence on the bi-modal wake dynamics of square-back bluff body," Phys. Fluids **35**(1), 015158 (2023).
[72]S. Han, F. Wang, and J. Zhang, "Influence of inflow conditions on simplified heavy vehicle wake," Phys. Fluids **36**(4), 045151 (2024).
[73]P. A. Montenegro, D. Barbosa, H. Carvalho, and R. Calcada, "Dynamic effects on a train-bridge system caused by stochastically generated turbulent wind fields," Eng. Struct. **211**, 110430 (2020).